RESEARCH ARTICLE

Check for updates

Cyano-bridged {Ln$_2$^{III}Fe$_2$^{III}} molecular squares (Ln = Gd, Tb, Dy, Ho, and Er): tuning the slow magnetic relaxation and magnetocaloric effects in zero-dimensional lanthanide Prussian blue analogues

Maria-Gabriela Alexandru, [iD] [a] Diana Visinescu, [iD] *[b] Sergiu Shova,[c] Nicolas Moliner,[d] Mario Pacheco,[d,e] Miguel Julve†[d] and Francesc Lloret*[d]

An isostructural series of neutral cyano-bridged tetranuclear iron(III)–lanthanide(III) complexes of general formula {[Fe(htpzb)(CN)(μ-CN)$_2$]$_2$[Ln(dmbpy)$_2$(NO$_3$)(H$_2$O)]$_2$}·2CH$_3$CN·2H$_2$O [Ln = Gd (**1**), Tb (**2**), Dy (**3**), Ho (**4**), and Er (**5**); htpzb = hydrotris(pyrazolyl)borate and dmbpy = 4,4′-dimethyl-2,2′-bipyridine] was synthesized and structurally and magnetically characterized. Single-crystal X-ray analysis of **1–5** revealed the formation of neutral cyano-bridged {Fe$_2$^{III}Ln$_2$^{III}} complexes (Ln = Gd, Tb, Dy, Ho, and Er) of square-like topology that crystallize in the triclinic $P\bar{1}$ space group. Solid-state direct-current magnetic susceptibility analysis evidenced weak intramolecular antiferromagnetic Fe^{III}–Ln^{III} interactions in **1** (Ln = Gd) together with large local magnetic anisotropies from the Ln^{III} ion in **2–5** (Ln = Tb, Dy, Ho, and Er). Frequency-dependent alternating current magnetic susceptibility signals occurred for **1–5** under an applied dc magnetic field of H = 1.0 (**1**) or 0.5 T (**2–5**), indicating field-induced slow magnetic relaxation effects typical of single-molecule magnets. Depending on the non-Kramer (Tb, Ho) or Kramer (Gd, Dy, Er) nature of the Ln^{III} ion, a single magnetic relaxation process *via* Orbach or Raman mechanism (**2** and **4**) or a multiple magnetic relaxation process that combines Orbach or Raman plus quantum tunneling of magnetization and/or direct (**1**, **3**, and **5**) mechanisms occurred along this series. **1–5** showed large magnetocaloric effects with a high to moderate maximum value of the magnetic entropy change at optimum working temperatures just above He liquefaction [−ΔS_{max} = 16.51 (**1**), 5.42 (**2**), 6.02 (**3**), 4.56 (**4**), and 5.86 J kg^{-1} K^{-1} (**5**) for H = 5 T at T_{opt} = T_{max} = 2 (**1**), 4 (**2**, **3** and **5**), and 6 K (**4**)], as well as a high to moderate magnetocaloric index at rather low optimum working fields [MCI = 6.4 (**1**), 3.3 (**2**), 4.7 (**3**), 0.9 (**4**), and 3.6 J kg^{-1} K^{-1} T^{-1} (**5**) for H_{opt} = H_{max} = 1.0 (**1**), 0.6 (**2**), 0.4 (**3**), 0.8 (**4**), and 0.6 T (**5**) at T = 2 K].

^{a}*Department of Inorganic Chemistry, Physical Chemistry and Electrochemistry, Faculty of Chemical Engineering and Biotechnologies, National University of Science and Technology Politehnica of Bucharest, 1-7 Gh. Polizu Street, 011061 Bucharest, Romania*

^{b}*Coordination and Supramolecular Chemistry Laboratory, Ilie Murgulescu Institute of Physical Chemistry, Romanian Academy, Splaiul Independentei 202, Bucharest 060021, Romania. E-mail: dianavisinescu@icf.ro*

^{c}*Petru Poni Institute of Macromolecular Chemistry, Romanian Academy, Aleea Grigore Ghica Vodă 41-A, RO-700487 Iasi, Romania*

^{d}*Departament de Química Inorgànica/Instituto de Ciencia Molecular, Universitat de València, C/Catedrático José Beltrán 2, 46980 Paterna, València, Spain. E-mail: francisco.lloret@uv.es*

^{e}*Facultad de Química, Universidad de la República, Av. Gral. Flores 2124, 11800 Montevideo, Uruguay*

† Passed away, July 2024.

Introduction

Cyano-bridged metal complexes represent a dynamic and resourceful class of multifunctional molecular materials unveiling new facets that have continuously expanded their area of application in thermo-,[1–3] photo-,[4,5] and electrocatalysis,[6] host–guest chemistry,[7] energy storage,[8–10] optical sensing,[11] and thermometry[12] among others. More specifically, magnetic molecules containing transition metal ions linked by the light, asymmetric CN$^-$ ligand, with a strong σ-donor and π-acceptor character, have been particularly attractive in magnetochemistry, as unique examples of cyano-bridged mixed-3d/nd molecule-based magnetic materials, so-called low-dimensional Prussian blue analogues (PBA).[13,14] In the past decade, however, the interest in this field is moving toward the related rare-earth hexacyanometallate derivatives, referred to as

3170 | *Inorg. Chem. Front.*, 2026, **13**, 3170–3185

This journal is © the Partner Organisations 2026

lanthanide Prussian blue analogues (Ln PBA).[15–23] This family of neutral or anionic cyano-bridged mixed-3d/4f molecule-based magnetic materials combine the intrinsic chemical versatility and structural stability of PBAs with the magnetic and magnetocaloric or optical (luminescent) properties of the lanthanide ions along with the redox and/or catalytic activities of the diamagnetic or paramagnetic first-row transition metal ions (and, occasionally, the organic ligands).

The high-spin ground state together with the large magnetic anisotropy exhibited by the majority of the lanthanide(III) ions, other than gadolinium(III), are crucial factors for the occurrence of the slow magnetic relaxation (SMR) effects in single-ion/molecule/chain magnets (SIM/SMM/SCM).[21–23] Otherwise, the isotropic gadolinium(III) ion, with a large spin ground state (S_{Gd} = 7/2), has been intensively exploited in molecular magnetic coolants because of its large magnetocaloric effects (MCE). Lanthanide metal complexes have therefore become promising components in the development of emerging technologies like quantum information processing (QIP) or molecular spintronics,[24,25] and adiabatic demagnetization refrigeration (ADR).[26–29] The assembly of high-nuclearity isotropic Gd^{III} complexes or mixed M^{III}–Gd^{III} derivatives, with a large change of magnetic entropy ($-\Delta S_m$) with the magnetic field sweeps (ΔH) at ultra-low temperature (below liquid He) is an important topic in ADR.[26–29] Conversely, the anisotropic Ln^{3+} complexes were rarely investigated in conventional ADR.[30–39] Likewise, the nd/4f heterometallics were appealing for the investigation of MCE,[40–42] and the cyano-bridged complexes of transition and lanthanide(III) cations provide a largely unexplored area of study.[43]

The rich library of heteroleptic polycyanometallate mononuclear complexes, with two-/three-/four- and five CN^- groups substituted with several blocking ligands, was the subject of several review papers[44–51] that highlighted their efficiency in acting as metalloligands to obtain low-dimensional heterobi-[44–49] and trimetallic cyano-bridged nd/nd′ coordination compounds.[50,51] In contrast, cyano-bridged 3d/4f coordination compounds were much less studied. For example, the reaction of tri- or tetracyanometallates with Ln^{3+} ions, capped with solvent molecules or chelating ligands, afforded a large variety of low-dimensional Ln PBAs, from: 0D oligonuclear complexes,[52,53] 1D[54–56] and 2D[56] coordination polymers. Focusing on cyano-bridged 3d/4f tetranuclear complexes, only the low-spin (LS) [Fe^{III}(bpy)(CN)$_4$]$^-$ (bpy = 2,2′-bipyridine)[53] as well as [Fe^{III}(htpzb)(CN)$_3$]$^-$ complex anions [htpzb = hydrotris(pyrazolyl)borate][57–60] led to square-like {Fe^{III}(LS)$_2$Ln$_2^{III}$} motifs. Our work on cyano-bridged molecular squares brought magnetic insights for the related series of general formula {[Fe^{III}(htpzb)]$_2$[Ln^{III}(NO$_3$)$_x$(pyim)$_y$(Ph$_3$PO)$_z$]$_2$} [Ln = La (x = 1, y = 2, z = 0); Ln = Gd, Tb, and Dy (x = 1, y = 1, z = 0); Ln^{III} = Ce, Eu, Sm, Pr, Nd, Gd, Tb, Dy, and Er (x = 1, y = 1, z = 1); pyim = 2-(1H-imidazol-2-yl)pyridine; Ph$_3$PO = triphenylphosphine oxide] showing a weak antiferromagnetic exchange interaction between Fe^{III}(LS) and Ln^{III} ions through the cyanide bridge (Ln = Eu, Sm, Nd, Gd, Tb, Dy, and Er).[57–59] SMR occurred for the Tb^{3+}, Dy^{3+} and Er^{3+} derivatives including

pyim and PPh$_3$O as capping ligands, showing how small changes in the Ln^{III} coordination sphere can suppress quantum tunneling effects to generate 3d/4f SMMs.[59]

Cyano-bridged 3d/4f square-like motifs were also assembled from ion(III) hexacyanometallates and Ln(III) ions capped with bidentate o-phenatroline or tridentate 2,2′:6′,2″-terpyridine ligands.[61–63] However, the simultaneous employment of two structure control elements, tricyanometallates as bis-monodentate angular connector and auxiliary bidentate blocking ligands (e.g., pyim) on coordination sites of Ln^{III} ions to prevent polymerization, proved to be a robust approach to achieve cyano-bridged mixed-3d/4f squares as unique examples of 0D Ln PBAs. Besides, the inclusion of an additional flexible coligand (e.g., Ph$_3$PO) allowed the fine tuning of the lanthanide(III) environment that could further influence the magnetic behavior of the tetranuclear square complex. Therefore, we envisaged to extend the cyano-bridged square-shaped family of {Fe^{III}(LS)$_2$Ln$_2^{III}$} complexes by using sterically hindered bipyridine-type chelating organic molecules as capping ligands of Ln^{III} coordination sites. Herein, we report on the new cyano-bridged square-shaped tetranuclear complexes of general formula {[Fe(htpzb)(CN)(μ-CN)$_2$]$_2$[Ln(dmbpy)(NO$_3$)$_2$(H$_2$O)]$_2$}·2CH$_3$CN·2H$_2$O [Ln = Gd (1), Tb (2), Dy (3), Ho (4), and Er (5); htpzb = hydrotris(pyrazolyl)borate and dmbpy = 4,4′-dimetyl-2,2′-bipyridine]. Besides the static and dynamic magnetic properties, we also examined the magnetocaloric properties of 1–5 to determine the influence of the nature of the Ln^{III} ion (Ln = Gd, Tb, Dy, Ho, and Er) on the spin dynamics and thermodynamics of the resulted {Fe^{III}(LS)$_2$Ln$_2^{III}$} complexes.

Experimental

Materials

Ln(NO$_3$)$_3$·6H$_2$O, dmbpy and acetonitrile were purchased from commercial sources and used as received. Ph$_4$P[Fe(htpzb)(CN)$_3$]·H$_2$O was prepared as described in the literature.[64]

Synthesis of the compounds

1–5 were prepared by following the same general method: an acetonitrile solution (20 cm^3) of Ph$_4$P[Fe(htptz)(CN)$_3$]·H$_2$O (0.067 mmol) was poured into an acetonitrile solution (20 cm^3) containing dmbpy (0.067 mmol), and the corresponding lanthanide salt, Ln(NO$_3$)$_3$·xH$_2$O (0.067 mmol) [Ln^{III} = Gd, 1 (x = 6); Tb, 2 (x = 6); Dy, 3 (x = 5); Ho, 4 (x = 6); Er, 5 (x = 6)]. The slow evaporation of the resulting red-orange solutions at room temperature afforded red-colored plates of 1–5 after one week. All the isolated crystalline products were air stable. Yield: 50 (1), 45 (2), 60 (3), 40 (4), 80 (5). Anal. calcd for C$_{52}$H$_{58}$N$_{28}$B$_2$O$_{16}$Fe$_2$Gd$_2$ (1): C, 35.07; H, 3.26; N, 22.03; found: C, 35.31; H, 3.28; N, 22.14%. C$_{52}$H$_{58}$N$_{28}$B$_2$O$_{16}$Fe$_2$Tb$_2$ (2): C, 35.00; H, 3.25; N, 22.67; found: C, 35.30; H, 3.19; N, 22.63%. C$_{52}$H$_{58}$N$_{28}$B$_2$O$_{16}$Fe$_2$Dy$_2$ (3): C, 34.86; H, 3.24; N, 21.90; found: C, 35.04; H, 3.19; N, 22.06%. C$_{52}$H$_{57}$N$_{28}$B$_2$O$_{15.5}$Fe$_2$Ho$_2$ (4): C, 34.94; H, 3.19; N, 21.95; found: C, 35.03; H, 3.15; N, 22.08%.

This journal is © the Partner Organisations 2026

Inorg. Chem. Front., 2026, 13, 3170–3185 | 3171

$C_{52}H_{57}B_2N_{28}O_{15.5}Fe_2Er_2$ (**5**): C, 34.85; H, 3.18; N, 21.89; found: C, 34.89; H, 3.14; N, 21.95%. Selected IR peaks (cm^{-1}, KBr pellets): 2149(m) (**1**), 2153(s) and 2123(m) (**2**), 2153(s) and 2122(m) (**3**), 2155(s) and 2123(m) (**4, 5**) [ν(C≡N)].

Physical techniques

Elemental analyses (C, H, N) and energy dispersive X-ray (EDX) analyses (Fe, Ln) for **1–5** were performed using a PerkinElmer 2400 analyzer and a Philips XL-30 scanning electron microscopy (SEM), respectively. The infrared spectra of **1–5** were recorded on a FTIR Bruker Tensor V-37 spectrophotometer using KBr pellets in the range 4000–400 cm^{-1}. UV-Vis spectra (diffuse reflectance technique) were recorded on a 220–1000 nm domain with a JASCO V-770 spectrophotometer, using MgO as the standard. Powder X-ray diffraction (XRD) measurements of powdered samples of **1–5** were collected at room temperature on a D8 Advance A25 Bruker diffractometer using graphite-monochromated Cu-K$_\alpha$ radiation (λ = 1.54056 Å).

Magnetic measurements

Direct current (dc) magnetic susceptibility and magnetization measurements were carried out on crushed crystals of **1–5** (mixed with grease to avoid any crystallite orientation) by using a Quantum Design MPMSXL-5 SQUID magnetometer. The dc magnetic susceptibility measurements were performed in the temperature ranges 2.0–300 K and under applied dc magnetic fields of 0.5 (T > 25 K) and 0.01 T ($T \leq$ 25 K) to prevent for saturation effects at low temperature. Magnetization measurements were performed in the temperature and field ranges of 2.0–10 K and 0–5 T, respectively, under steps of 1 K and 0.2 T. Alternating current (ac) magnetic susceptibility measurements were recorded with a Quantum Design Physical Property Measurement System (PPMS) in the temperature range 2.0–10 K under ±3.95 G oscillating field at frequencies in the range 1.0–10.0 kHz, both in zero dc field and under applied dc fields of 1.0 (**1**) or 0.5 T (**2–5**). The magnetic susceptibility data were corrected for the diamagnetism of the constituent atoms and the sample holder (a plastic bag).

Crystallographic data collection and structure determination

Crystallographic measurements for **1–5** were carried out with an Oxford-Diffraction XCALIBUR E CCD diffractometer equipped with graphite-monochromated Mo Kα radiation. The unit cell determination and data integration were carried out using the CrysAlisPro package from Oxford Diffraction.[65] The structures were solved with SHELXT program using the intrinsic phasing method and refined by the full-matrix least-squares method on F^2 with SHELXL.[66,67] Olex2 was used as an interface to the SHELX programs.[68] Non-hydrogen atoms were refined anisotropically. Hydrogen atoms attached to carbon were added in idealized positions and refined using a riding model. The hydrogen atoms of the OH groups were located from difference Fourier maps and their positions were refined in agreement with the H-bonds parameters. The main crystal-

lographic data together with structure solution and refinement details are summarized in Table 1 and the corresponding CIF-files. The structural images were obtained with the Diamond 4 program.[69] The unit cell parameters and refinement conditions for **1–5** are given in Table 1. CCDC 2504399 (**1**), 2504400 (**2**), 2504401 (**3**), 2504402 (**4**), 2504403 (**5**).

Results and discussion

Synthesis and general physicochemical characterization

The stoichiometric reaction of the anionic [Fe^{III}(htpzb)(CN)$_3$]$^-$ metalloligand and the preformed [Ln^{III}(dmbpy)(NO$_3$)$_2$(H$_2$O)]$^+$ (Ln = Gd, Tb, Dy, Ho, and Er) complex cation (1 : 1 : 1 Fe^{III}/Ln^{III}/dmbpy molar ratio) in acetonitrile solution, at room temperature, afforded X-ray quality crystals of the isostructural series of heterometallic complexes **1–5**. They were characterized by elemental (C, H, N) and EDX analyses, as well as FT-IR spectroscopy and powder XRD (see Experimental section).

The estimated value of the Fe : Ln molar ratio for **1–5** from EDX analyses is 1 : 1, in agreement with the proposed chemical formula determined from elemental analyses. The FT-IR spectra of **1–5** are very similar and support the formation of cyano-bridged {Fe^{III}(LS)$_2$Ln$_2^{III}$} complexes (Fig. S1–S5 in SI), through two distinct broad absorptions peaks at energies ranging from 2149–2155 and 2122–2123 cm^{-1} corresponding to the stretching vibrations of the bridging and terminal cyanide ligands, respectively, of the [Fe^{III}(htpzb)(CN)(μ-CN)$_2$]$^-$ units. The C–H stretching and ring stretching modes of htpzb and dmbpy ligands cover the range 2950–2750 cm^{-1} and 1650–1410 cm^{-1}, respectively. The broad and medium intensity band in the range 2514–2553 cm^{-1} is characteristic for the B–H stretching vibration from the htpzb ligand. For **1–5**, the coordinated nitrato ligands were also identified as a strong and broad absorption at ca. 1384–1387 cm^{-1}, as well as a medium intensity band at ca. 812–816 cm^{-1}.[70] The solid-state UV-Vis spectra for **1–5** are shown in Fig. S6 in SI and exhibit similar profiles, with a UV band centered at approximately 300 nm, as well as a broad absorption covering the visible region. The intense UV absorption band likely envelops n/π–π⋆ transitions of the dmbpy ligand, as well as ligand-to-metal charge transfer (LMCT) from the cyanide ligands to LSFe^{III} center.[71] The broad and intense absorption at ca. 600 nm could be generated by LMCT transitions (htpz → LSFe^{III}, with a shoulder at ca. 430 nm) and metal to ligand charge transfer (MLCT) transitions within the {Fe^{III}(htpzb)(CN)$_3$} unit, which likely mask the characteristic, very weak, sharp absorptions of Ln^{III} ions.

The purity of bulk samples of **1–5** was confirmed by the agreement between their experimental and simulated powder XRD patterns (see Fig. S7–S11 in the SI).

Description of the structures

1–5 are isostructural crystallizing in the triclinic $P\bar{1}$ space group (Table 1). Selected crystallographic and structural data for **1–5** are given in Tables 1 and 2.

3172 | *Inorg. Chem. Front.*, 2026, **13**, 3170–3185

This journal is © the Partner Organisations 2026

Table 1 Crystallographic data and structure refinement parameters for **1–5**

	1	**2**	**3**	**4**	**5**
Formula	$C_{52}H_{58}N_{28}B_2O_{16}Fe_2Gd_2$	$C_{52}H_{58}N_{28}B_2O_{16}Fe_2Tb_2$	$C_{52}H_{58}N_{28}B_2O_{16}Fe_2Dy_2$	$C_{52}H_{57}N_{28}B_2O_{15.5}Fe_2Ho_2$	$C_{52}H_{57}B_2N_{28}O_{15.5}Fe_2Er_2$
Fw	1779.08	1782.42	1789.58	1785.43	1790.09
T [K]	180.05(10)	159.8(10)	149.9(2)	293(2)	293(2)
Space group	$P\bar{1}$	$P\bar{1}$	$P\bar{1}$	$P\bar{1}$	$P\bar{1}$
a [Å]	11.6608(4)	11.6335(4)	11.6345(4)	11.6557(3)	11.6406(4)
b [Å]	11.7464(3)	11.7416(5)	11.7335(4)	11.8334(3)	11.8371(4)
c [Å]	13.5504(4)	13.4857(4)	13.4726(5)	13.6036(6)	13.5872(5)
α [°]	72.921(2)	72.912(3)	72.844(3)	72.838(3)	72.779(3)
β [°]	77.362(3)	77.393(3)	77.299(3)	77.133(3)	77.078(3)
γ [°]	74.728(3)	74.761(3)	74.785(3)	74.905(3)	74.954(3)
V [Å^3]	1691.28(9)	1678.88(12)	1675.39(11)	1709.13(11)	1704.96(11)
Z	1	1	1	1	1
ρ_{calc} [g cm^{-3}]	1.747	1.763	1.774	1.735	1.743
μ [mm^{-1}]	2.442	2.591	2.716	2.790	2.937
Crystal size [mm]	0.25 × 0.15 × 0.05	0.15 × 0.1 × 0.03	0.3 × 0.2 × 0.1	0.25 × 0.15 × 0.1	0.3 × 0.3 × 0.25
2θ range	1.8290–28.9430	1.8310–28.7070	1.8650–29.1090	1.8300–25.5280	1.6130–28.5870
Refls collected	14 964	15 418	11 654	12 538	12 593
Indep. refls, R_{int}	5416, 0.0386	5240, 0.0443	5448, 0.0353	5028, 0.0441	5394, 0.0327
Data/rests/ params	5892/0/464	5893/7/475	5882/0/467	6000/0/464	5952/0/464
GOF	1.059	1.029	1.074	1.016	1.039
R_1, wR_2 (all data)	R_1 = 0.0312 wR_2 = 0.0573	R_1 = 0.0383 wR_2 = 0.0666	R_1 = 0.0353 wR_2 = 0.0627	R_1 = 0.0535 wR_2 = 0.0672	R_1 = 0.0334 wR_2 = 0.0570
CCDC no.	2504399	2504400	2504401	2504402	2504403

Table 2 Selected intra- and intermolecular distances and angles for **1–5**

	1	**2**	**3**	**4**	**5**
Ln1–Fe1–Ln1a ^{a} (°)	96.34	96.18	96.22	97.16	97.16
Fe1–Ln1–Fe1a ^{a} (°)	83.66	83.82	83.78	82.84	82.84
Fe–C$_{cyanide}$ (Å)	1.914(3)–1.936(4)	1.921(4)–1.935(5)	1.922(4)–1.941(4)	1.927(6)–1.933(5)	1.929(4)–1.934(4)
Fe–N$_{pyrazolyl}$ (Å)	1.970(2)–1.998(3)	1.968(3)–1.994(3)	1.971(3)–1.997(3)	1.972(4)–1.996(4)	1.974(3)–1.998(3)
(Fe1–C–N)$_{br}$ ^{b} (°)	176.1(3)/178.3(3)	177.9(4)/175.8(4)	178.5(3)/175.6(4)	175.3(5)/177.0(5)	175.9(3)/178.6(3)
(Fe1–C–N)$_t$ ^{c} (°)	177.1(3)	177.1(3)	176.5(4)	178.5(5)	177.4(4)
Ln1–N$_{dmbpy}$ (Å)	2.486(3)/2.549(2)	2.467(3)/2.528(3)	2.454(3)/2.515(3)	2.448(4)/2.514(4)	2.427(3)/2.503(3)
Ln1–O$_{nitrate}$ (Å)	2.483(2)–2.522(2)	2.479(3)–2.512(3)	2.433(3)–2.508(3)	2.416(3)–2.516(3)	2.406(2)–2.512(2)
Ln1–O1 W (Å)	2.412(2)	2.386(3)	2.380(2)	2.384(3)	2.368(2)
(Ln1–N$_{cyanide}$)$_{br}$ ^{b} (Å)	2.454(3)/2.466(3)	2.449(3)/2.439(3)	2.440(3)/2.422(3)	2.409(5)/2.437(4)	2.403(3)/2.435(3)
(Ln1–N–C)$_{br}$ ^{b} (°)	168.7(3)/173.0(3)	168.8(3)/173.6(3)	169.3(3)/174.3(3)	171.3(4)/175.1(4)	171.0(3)/174.2(3)
Fe1···Ln1/Fe1a···Ln1 ^{a} (Å)	5.50	5.48/5.49	5.47/5.48	5.47/5.50	5.46/5.49
(π···π)$_{pyrazolyl}$ (Å/°)	3.60 Å/13.59	3.39 Å/17.37 and 17.38	3.39 Å/17.46	3.44/19.12	3.44/19.08
(π···π)$_{dmbpy}$ (Å/°)	3.80/23.57, 22.19	3.80/22.31, 23.98	3.80/22.64, 24.35	3.90/23.75, 24.76	3.91/24.09, 24.93
(C–H···π)$_{pyrazolyl}$ (Å)	2.72 Å	2.78	2.79	2.87	2.88
Fe1···Fe1b via (π···π)$_{pyrazolyl}$ contacts^a (Å)	7.73	8.01	8.02	8.13	8.14
Ln1···Ln1c (H-bonds)^a (Å)	6.53	6.51	6.50	6.56	6.56

^{a} Symmetry codes: (a) = 1 − x, 1 − y, 1 − z (**1**, **3–5**), 1 − x, 1 − y, 2 − z (**2**); (b) = 1 + x, y, z (**1**, **3–5**), −1 + x, y, z (**2**); (c) = 1 − x, 1 − y, 2 − z (**1**, **3–5**), 1 − x, 1 − y, 1 − z (**2**). ^{b} br – bridging. ^{c} t – terminal.

The crystal structure of **1–5** consists of a neutral, centrosymmetric cyano-bridged heterotetranuclear unit of square topology, {[Fe(htpzb)(CN)(μ-CN)$_2$]$_2$[Ln(dmbpy)(NO$_3$)$_2$(H$_2$O)]$_2$} [Ln = Gd (**1**), Tb (**2**), Dy (**3**), Ho (**4**), and Er (**5**)] (see Fig. 1 and Fig. S12a–S15a in SI), together with two acetonitrile and two water molecules of crystallization. Bond lengths and angles for **1–5** are gathered in Tables S1 and S2 in SI. Water and acetonitrile crystallization molecules are connected through O–H···O and O–H···N hydrogen bonds to the terminal CN⁻ and NO$_3$⁻ ligands (Fig. S12a–S15a in SI).

The {Fe$_2^{III}$Ln$_2^{III}$} entity in **1–5** is assembled from two bis-monodentate, anionic [Fe^{III}(htpzb)(CN)(μ-CN)$_2$]⁻ and two coordinatively unsaturated, cationic [Ln^{III}(dmbpy)(NO$_3$)$_2$(H$_2$O)]⁺ units. The *cis*-orientation of two CN⁻ bridging ligands of the *fac*-[Fe^{III}(htpzb)(CN)$_3$]⁻ complex anion, together with the complementary labile/free coordination sites on [Ln^{III}(dmbpy)(NO$_3$)$_2$(H$_2$O)]⁺ complex cation, gave rise to a cyclic distorted square-shaped molecule, the two Fe^{III} and Ln^{III} ions filling alternatively the corners of the square. The Ln1–Fe1–Ln1a and Fe1–Ln1–Fe1a angles in **1–5** vary in the ranges 96.18–97.16

This journal is © the Partner Organisations 2026

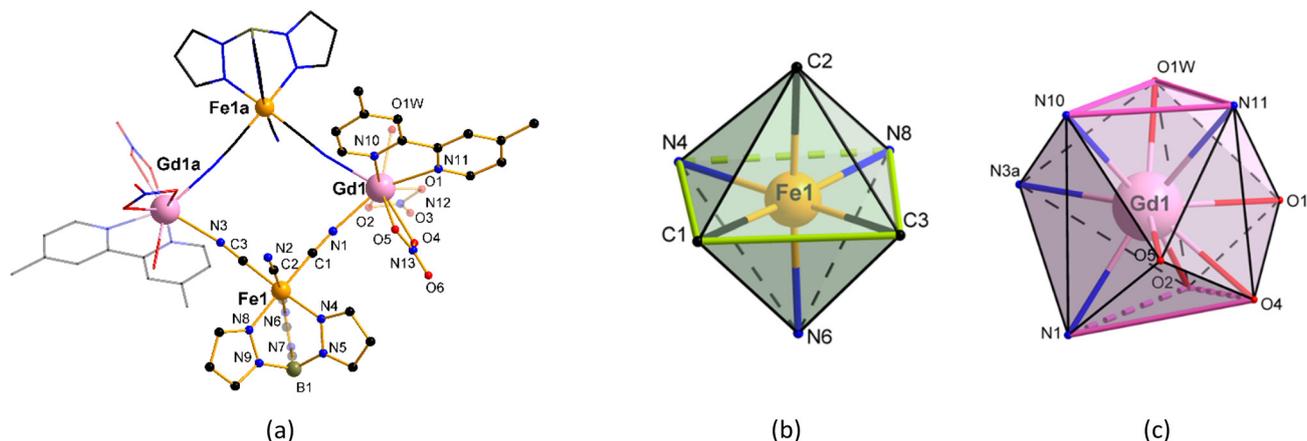*Inorg. Chem. Front.*, 2026, **13**, 3170–3185 | **3173**

Fig. 1 (a) View of the square-shaped cyano-bridged heterotetranuclear unit in **1** together with the atom labelling scheme [symmetry code: (*a*) = 1 − *x*, 1 − *y*, 1 − *z*]. The water and acetonitrile crystallization molecules were omitted for the sake of clarity. (b) The octahedral surrounding of Fe^{III} ion. (c) Distorted tricapped trigonal prism geometry of Gd^{III} ion.

and 82.84–83.82°, respectively, the degree of rhombic distortion being consistent with previous reports.[53,57–59]

Each crystallographically independent iron(III) ion from **1**–**5** is six-coordinated by three carbon atoms belonging to CN⁻ ligands, disposed in a *fac*-arrangement, and three nitrogen atoms from the three pyrazolyl rings of the htpzb ligand, in a slightly distorted octahedral metal surrounding [CShM = 0.153 (**1**), 0.156 (**2**), 0.148 (**3**), 0.129 (**4**), and 0.126 (**5**), see Fig. 1b, Fig. S12b–S15b and Table S3 in SI].[72,73] The Fe–C and Fe–N bond lengths are similar in **1**–**5**, ranging from 1.914(3)–1.941 (4) and 1.968(3)–1.998(3) Å, respectively (Table 2). As far as the Fe–C–N angles from the bridging and terminal cyanide ligands are concerned, their values are close to linearity in **1**–**5**, ranging from 175.3(5)–178.6(3) and 176.5(4)–178.5(5)°, respectively (Table 2). All these values related to the iron(III) surrounding are close to those previously reported for the cyano-bearing [Fe^{III}(htpzb)(CN)$_3$]⁻ moiety in the related homotetranuclear iron(III) complex.[74] The two distinct Fe^{III}···Ln^{III} intermetallic distances through the CN⁻ bridges in **1**–**5** range between 5.46–5.50 Å (Table 2) which are similar to previously reported cyano-bridged {LSFe^{III}Ln^{III}}$_2$ squares.[53,57–59] On the other hand, each crystallographically independent lanthanide(III) ion in **1**–**5** is capped by two N atoms from one dmbpy and four O atoms from two nitrato chelating ligands, the coordination sphere being completed by two N atoms from the CN⁻ bridges and one O atom from the aqua ligand (see Fig. 1c, Fig. S12c–S15c and Table S3 in SI).

The donor atoms around the Ln^{III} ions in **1**–**5** describe a nine-coordinated polyhedron with a geometry close to distorted tricapped trigonal prism (TCTPR) of D_{3h} symmetry, estimated through SHAPE 2.1 software [CShM = 1.900 (**1**), 1.829 (**2**), 1.774 (**3**), 1.744 (**4**), and 1.738 (**5**), see Table S3 in SI], so that the deviations from ideal TCTPR geometry decrease with increasing the number of 4f electrons along this series (*n* = 7–11).[72,73]

It is worth mentioning that, in the earlier examples of cyano-bridged {LSFe^{III}Ln^{III}}$_2$ squares, the nine-coordinated sur-

rounding of Ln^{III} ions is either distorted monocapped square antiprism[53] or muffin-like.[57–59] The bite angles of the dmbpy and nitrato chelating ligands in **1**–**5** are within the ranges 64.68(8)–66.22(10) and 51.38(7)–52.66(12)°, respectively (Table 2), being the main source of the polyhedron distortion from ideal tricapped trigonal prism.

The Ln1–N$_{dmbpy}$ distances in **1**–**5** are in the range 2.427(3)–2.528(3) Å, being higher than those corresponding to the bridging cyanide ligands in the range 2.403(3)/2.466(3) Å (Table 2). Also, the Ln1–N$_{dmbpy}$ bond lengths correspond well to the previously published examples including similar fragments.[75–79] The two Ln1–N1–C1 and Ln1–N2a–C2a angles involving the bridging cyanide ligands in **1**–**5**, slightly deviate from linearity, being in the ranges of 168.7(3)–175.1(4)°, as other reports of cyano-bridged {LSFe^{III}Ln^{III}}$_2$ squares.[53,57–59] Also, the Ln1–O1W distance in the range 2.368(2)–2.412(2) Å is shorter than the Ln1–O bond lengths from nitrate that vary in the range 2.406(2)–2.522(2) Å (Table 2, symmetry codes (*a*) = 1 − *x*, 1 − *y*, 1 − *z* for **1**, **3**–**5** and (*a*) = 1 − *x*, 1 − *y*, 2 − *z* for **2**). Overall, the average values of the Ln1–N$_{dmbpy}$, Ln1–N$_{CN}$, Ln1–N$_{nitrate}$, Ln1–O$_{nitrate}$, and Ln1–OW distances decrease with the number of 4f electrons along this series (*n* = 7–11), as expected from the well-known "lanthanide contraction" phenomenon.

In the crystal lattice of **1**–**5**, the {Fe$_2^{III}$Ln$_2^{III}$} entities are further interconnected through non-covalent, hydrogen bonding, π···π, and C–H···π interactions to build a three-dimensional supramolecular network (see Fig. 2 and Fig. S16–S23 in SI). The adjacent {Fe$_2^{III}$Ln$_2^{III}$} entities are linked *via* O$_{aqua}$–H···N and C–H···O$_{nitrate}$ hydrogen bonds involving the crystallization acetonitrile molecules and the peripheral aqua and nitrate ligands, respectively (Table S4 in SI), developing supramolecular double-chains running parallel to the crystallographic *a* axis (Fig. 2, top and Fig. S16–S19 in SI). Besides, π···π and C–H···π stacking interactions established between pyrazolyl rings of htpzb ligands belonging to neighboring {Fe$_2^{III}$Ln$_2^{III}$} entities of **1**–**5** consolidate the supramolecular
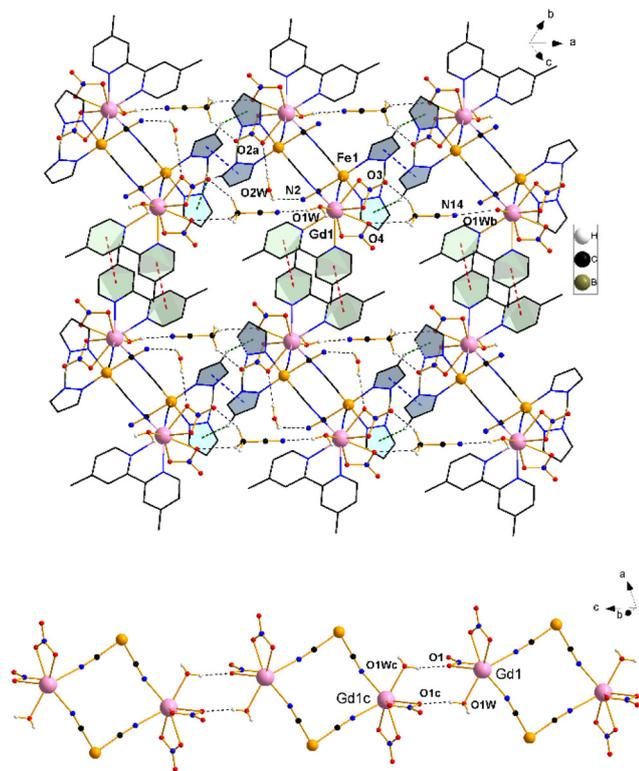
Fig. 2 Top: View of a fragment of the crystal packing showing the layers formed by O···O type H-bonds, C−H···π and π···π stacking interactions established between the pyrazolyl rings for **1** [one pyrazolyl ring and the terminal cyanide ligand were removed for the sake of clarity, symmetry codes: (a) = 1 − x, 1 − y, 1 − z, (b) = 1 + x, y, z]. Bottom: View along the crystallographic c axis showing the H-bonds (black dotted lines) established between peripheral aqua (O1W) and nitrate ligands (O2) in **1**. The htpzb, dmbpy and the terminal cyanide ligands, as well as the crystallization water and acetonitrile molecules were omitted for the sake of clarity [symmetry code: (c) = 1 − x, 1 − y, 2 − z].

double-chains (the centroid···centroid distance and the angles between the normal to the ring and the centroid–centroid vector are in the ranges 3.39–3.60 Å and 13.59–19.12°, while the C–H···π distances are in the range 2.72–2.88 Å, Table 2). Offset π···π stacking interactions are established between the pyridyl rings of the outer dmbpy ligands assembling supramolecular layers in the ac crystallographic plane. The neighboring layers interact further along c axis through H-bonds established between peripheral aqua and nitrate ligands to build a 3D supramolecular network (see Table S3, Fig. 2, bottom and Fig. S20–S23 in SI). The closest intermetallic Fe1···Fe1b distance in **1–5** across $(\pi \cdots \pi)_{pyrazolyl}$ contacts is in the range 7.73–8.14 Å, whereas the smallest Ln1···Ln1c distance across the H-bonds is in the range 6.50–6.56 Å (Table 2).

Magnetic properties

The magnetic properties of **1–5** have been investigated, both in the dc and ac regimes, to unveil the influence of the spin ground state and magnetic anisotropy of the Ln^{III} ion (Ln =

Gd, Tb, Dy, Ho, and Er) on the static and dynamic magnetic behavior of this series of cyano-bridged heterometallic $\{Ln_2^{III}Fe_2^{III}\}$ molecular squares as illustrative examples of 0D PBA (see Table S5 in SI).[53,57–60]

Static dc magnetic behavior. The dc magnetic properties of **1–5** in the form of $\chi_M T$ vs. T (χ_M being the dc molar magnetic susceptibility per $\{Ln_2^{III}Fe_2^{III}\}$ unit and T the absolute temperature) and M vs. H plots (M being the molar magnetization per $\{Ln_2^{III}Fe_2^{III}\}$ unit and H the applied dc magnetic field) are depicted in Fig. 3, while the normalized M vs. H/T plots are represented in Fig. S24 in SI. The static magnetic behavior of **2–5** are qualitatively similar, being different from that of **1**, as expected from the magnetically isotropic nature of the Gd^{III} ion compared to the other magnetically anisotropic Ln^{III} ions (Ln = Tb, Dy, Ho, and Er) resulting from their large spin–orbit coupling (SOC).
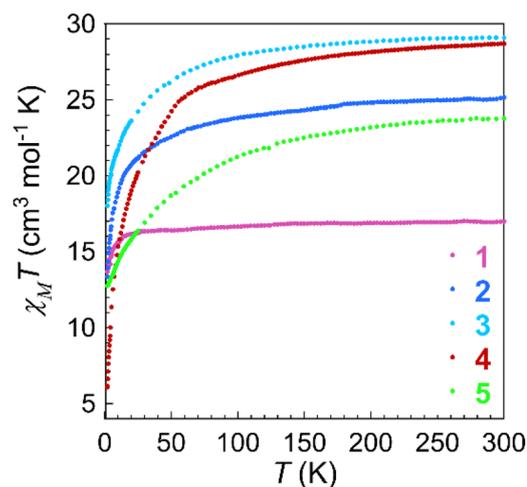
(a)
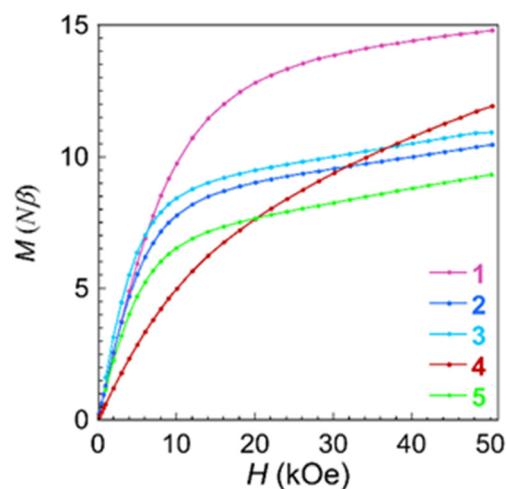
(b)

Fig. 3 (a) Temperature dependence of $\chi_M T$ for **1–5**. (b) Field dependence of M at 2 K for **1–5** (the solid lines are only eye-guides).

This journal is © the Partner Organisations 2026

Inorg. Chem. Front., 2026, **13**, 3170–3185 | **3175**

At room temperature, the $\chi_M T$ value of **1** is 16.70 cm^3 mol^{-1} K, a value which is close to the one expected for the sum of two magnetically isolated LS 3d^5 Fe^{III} ions (S_{Fe} = 1/2) with an unquenched orbital momentum ($^2T_{2g}$ term in O_h symmetry) plus two orbital free 4f^7 Gd^{III} ions (S_{Gd} = 7/2) with an $^8S_{7/2}$ ground state [$\chi_M T = 2 \times (N\beta^2 g_{Fe}{}^2/3k)S_{Fe}(S_{Fe} + 1) + 2 \times (N\beta^2 g_{Gd}{}^2/3k)S_{Gd}(S_{Gd} + 1) = 2 \times 0.46 + 2 \times 7.88 = 16.67$ cm^3 mol^{-1} K with g_{Fe} = 2.215 and g_{Gd} = 2.0] (Fig. 3a). In fact, the $^2T_{2g}$ term of the LS Fe^{III} ion in O_h symmetry is split under a rhombic distortion into a ground doublet state ($^2A_{1g}$) and two excited doublet states ($^2B_{1g}$ and $^2B_{2g}$).

Upon cooling, $\chi_M T$ decreases slightly and quasi-linearly down to 20 K due to the SOC effects of the LS Fe^{III} ions, below this temperature $\chi_M T$ abruptly falling down to reach a minimum value of 13.67 cm^3 mol^{-1} K at 2.0 K. This value is well below that expected for the sum of two magnetically isolated LS Fe^{III} ions at this low temperature plus two isotropic Gd^{III} ions ($\chi_M T = 2 \times 0.15 + 2 \times 7.875 = 16.05$ cm^3 mol^{-1} K) which unambiguously supports the occurrence of an antiferromagnetic interaction between the LS Fe^{III} and Gd^{III} ions through the cyanide bridge in **1**.

Hence, the maximum M value at 2 K for H = 5 T is 14.8$N\beta$ (Fig. 3b), which is below that expected for the sum of two Gd^{III} and two low-spin Fe^{III} ions, magnetically non-interacting [$M = 2 \times (g_{Fe}S_{Fe} + g_{Gd}S_{Gd})N\beta = 16.2N\beta$ (with g_{Gd} = 2.0 and g_{Fe} = 2.2)], being close to that of a tercet ground state [$S = 2(S_{Gd} - S_{Fe}) = 6$] resulting from the antiparallel alignment of the spin momenta of the LS Fe^{III} and Gd^{III} ions [$M = gSN\beta = 12.4N\beta$ with $g = (19/28)g_{Gd} + (9/28)g_{Fe} = 2.06$]. Moreover, the reduced isothermal magnetization curves from 2 up to 10 K are almost overlapped (Fig. S24a in SI), in agreement with the small, if not negligible, local magnetic anisotropy of the Gd^{III} ions.

On the other hand, the $\chi_M T$ values at room temperature for **2–5** are equal to 25.17 (**2**), 29.10 (**3**), 28.70 (**4**), and 23.79 cm^3 mol^{-1} K (**5**) (Fig. 3a). These values well correspond to the theoretical ones for the sum of two magnetically non-interacting LS 3d^5 Fe^{III} ions with a significant orbital contribution [$\chi_M T = 2 \times (N\beta^2 g_{Fe}{}^2/3k)S_{Fe}(S_{Fe} + 1) = 2 \times 0.46 = 0.92$ cm^3 mol^{-1} K with g_{Fe} = 2.215] plus two magnetically isolated 4f^8 Tb^{III} (**2**), 4f^9 Dy^{III} (**3**), 4f^{10} Ho^{III} (**4**), and 4f^{11} Er^{III} ions (**5**) with ($^7F_6$ (J_{Tb} = 6, L_{Tb} = 3, and S_{Tb} = 3), $^6H_{15/2}$ (J_{Dy} = 15/2, L_{Dy} = 5/2, and S_{Dy} = 5/2), $^5I_8$ (J_{Ho} = 8, L_{Ho} = 3/2, and S_{Ho} = 2), and $^4I_{15/2}$ ground states (J_{Er} = 15/2, L_{Er} = 3/2, and S_{Er} = 3/2) [$\chi_M T = 2 \times (N\beta^2 g_J{}^2/3k)J(J + 1) = 23.64$ (**2**), 28.34 (**3**), 28.14 (**4**), and 22.96 cm^3 mol^{-1} K (**5**) with g_J = 3/2, 4/3, 5/4, and 6/5, respectively], being well-separated from the first excited states that are then unpopulated in all the temperature range investigated. Upon cooling, $\chi_M T$ for **2–5** (Fig. 3a) continuously decreases down to ca. 150 K, below this temperature $\chi_M T$ sharply dropping to attain a minimum value of 13.36 (**2**), 18.04 (**3**), 6.10 (**4**), and 12.75 cm^3 mol^{-1} K (**5**) at 1.9 K. Overall, this magnetic behavior obeys to the occurrence of a large SOC of the magnetically anisotropic Ln^{III} ions (Ln = Tb, Dy, Ho, and Er) in **2–5**, together with an antiferromagnetic interaction between the LS Fe^{III} and Ln^{III} ions through the cyanide bridge, as observed in **1**. In fact, the isothermal magnetization curves for **2–5** at 2.0 K are far from

reaching saturation, and M attains maximum values of 10.46 (**2**), 10.92 (**3**), 11.92 (**4**), and 9.32$N\beta$ (**5**) for H = 5 T (Fig. 3b). These values are far below those expected for the corresponding ground states [$J = 2(J_{Ln} - S_{Fe})$ = 11 (**2**), 14 (**3**), 15 (**4**), and 14 (**5**)] resulting from the antiparallel alignment of the total momenta of the LS Fe^{III} and Ln^{III} ions [$M = g_J JN\beta$ = 19.15 (**2**), 22.88 (**3**), 23.76 (**4**), and 21.70 $N\beta$ (**5**) with g_J = 1.74, 1.63, 1.58, and 1.55, respectively]. Also, the reduced isothermal magnetization curves for **2–5** from 2 to 10 K did not collapse, indicating a significant local magnetic anisotropy of the Ln^{III} ions (Ln = Tb, Dy, Ho, and Er, see Fig. S24b–e in SI).

Dynamic magnetic behavior. The dynamic magnetic properties of **1–5** have been investigated by variable-temperature (T = 2.0–10 K) and variable-frequency (ν = 1–10 kHz) alternating current (ac) magnetic susceptibility measurements under an oscillating ac field of 5 Oe, both in the absence and the presence of an applied direct current (dc) field (see Experimental section).

The χ'_M and χ''_M vs. T plots of **1–5** (where χ'_M and χ''_M represent the in-phase and out-of-phase components of the molar ac magnetic susceptibility per {Ln$_2$Fe$_2^{III}$} unit) under an applied dc field (H) of 1.0 (**1**) or 0.5 T (**2–5**) are depicted in Fig. 4. No χ''_M signal occurred at zero dc field for any member of this series (data not shown), as expected for a fast magnetic relaxation due to the quantum tunneling of magnetization (QTM). Under a small dc field [H = 1.0 (**1**) and 0.5 T (**2–5**)], however, very weak but not negligible frequency-dependent χ''_M maxima appeared, which are indicative of a slow magnetic relaxation typical of field-induced SMMs. This situation contrasts with that found for the other reported examples of cyano-bridged {Fe$_2^{III}$Ln$_2^{III}$} squares, which only in a few cases show incipient frequency-dependent χ''_M signals, but with no maxima, in the presence of a small dc field (Table S5).[57–59] In particular, the isostructural series of complexes of general formula [Fe{hbpzb}(CN)(μ-CN)$_2$Ln(NO$_3$)$_2$(pyim)(Ph$_3$PO)]$_2$·2CH$_3$CN [Ln = Tb, Dy, and Er; hbpzb = hydrotris(pyrazolyl)borate, pyim = 2-(1H-imidazol-2-yl)pyridine, and Ph$_3$PO = triphenylphosphine oxide] showed very incipient χ''_M signals at H = 0.1 or 0.25 T.[59]

The magnetic relaxation times (τ) at H = 1.0 (**1**) or 0.5 T (**2–5**) can be alternatively calculated from the least-squares fitting of the respective χ'_M or χ''_M vs. ν plots through the generalized Debye model [eqn (1) and (2)] (Fig. S25 in SI).[80] The τ values calculated from the χ''_M vs. ν plots are fairly more accurate than those from the χ'_M vs. ν plots, as far as the magnetic relaxation rate is equal to the angular frequency of the oscillating ac field at the χ''_M maxima ($\tau^{-1} = \omega_{max} = 2\pi\nu_{max}$). They are represented in Fig. 5 in the form of the ln τ vs. 1/T (so-called Arrhenius) and ln τ vs. ln T plots. On the other hand, the χ''_M vs. χ'_M (so-called Cole–Cole or Argand) plots for **2–5** in the temperature range 2.0–6.0 K give almost perfect semicircles, while those for **1** in the temperature range 2.0–9.0 K yield minor arcs in the low-temperature range and semicircles above 6 K (Fig. S26 in SI). The adiabatic (χ_S) and isothermal (χ_T) magnetic susceptibilities as well as the exponential factor (α) for **1–5** were accurately obtained from the least-squares fitting of the respective Argand plots (Fig. S27 in SI).
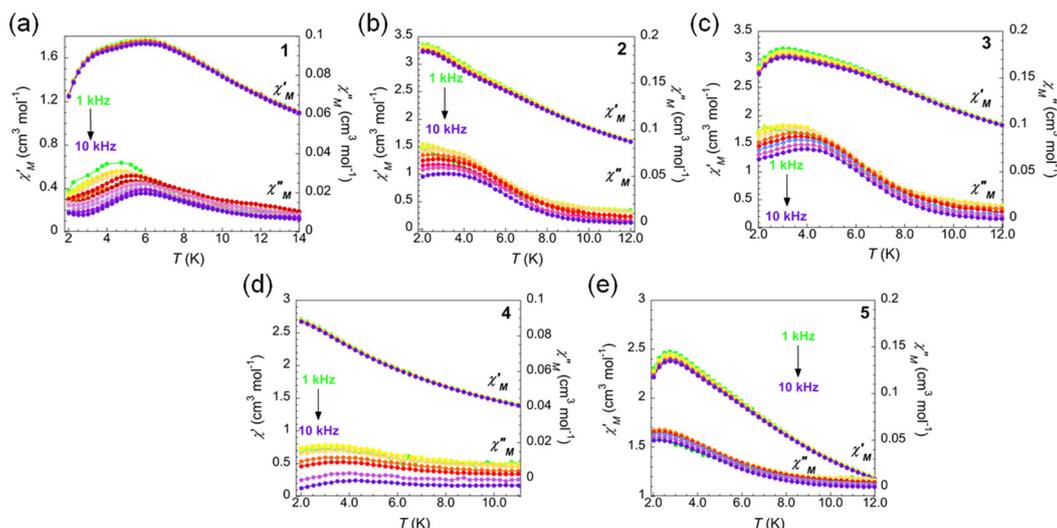
3176 | *Inorg. Chem. Front.*, 2026, **13**, 3170–3185

This journal is © the Partner Organisations 2026

Fig. 4 Temperature dependence of χ'_M and χ''_M (a–e) for **1–5** at ± 5 Oe oscillating field in the frequency range of 1.0–10.0 kHz (green to violet) and under applied static magnetic field of 1.0 (**1**) or 0.5 T (**2–5**). The solid lines are only eye-guides.
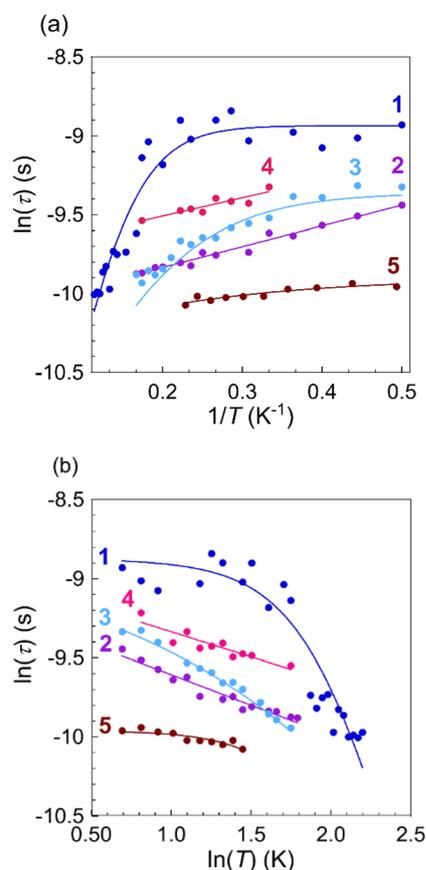

Fig. 5 Ln τ vs. 1/T (Arrhenius) (a) and ln τ vs. ln T (b) plots of τ for **1–5** under an applied dc field of 1.0 (**1**) or 0.5 T (**2–5**). The solid lines represent the best-fit curves for ORB (**2** and **4**) and ORB plus QTM (**1**, **3**, and **5**) mechanisms (a) or, alternatively, RAM (**2** and **4**) and RAM plus QTM and DIR (**1**, **3**, and **5**) mechanisms (b) (see text).

The relatively low values of the α parameter [$\alpha = 0.18$–0.65 (**1**)/0.15–0.41 (**2**)/0.32–0.41 (**3**)/0.23–0.47 (**4**)/0.20–0.31 (**5**); Fig. S27 in SI] supports a narrow distribution of τ values in the magnetic relaxation process for **1–5** typical of SMMs ($\alpha = 0$ and 1 for single and infinite relaxation processes, respectively).

$$\chi' = \chi_S + (\chi_T - \chi_S)[1 + (2\pi\nu\tau)^{(1-\alpha)} \sin(\alpha\pi/2)]/[1 + 2(2\pi\nu\tau)^{(1-\alpha)} \times \sin(\alpha\pi/2) + (2\pi\nu\tau)^{(2-2\alpha)}] \tag{1}$$

$$\chi'' = (\chi_T - \chi_S)(2\pi\nu\tau)^{(1-\alpha)} \cos(\alpha\pi/2)/[1 + 2(2\pi\nu\tau)^{(1-\alpha)} \sin(\alpha\pi/2) + (2\pi\nu\tau)^{(2-2\alpha)}] \tag{2}$$

$$\chi'' = (\chi_T - \chi_S)/2 \tan[(1+\alpha)\pi/2] + [(\chi' - \chi_S)(\chi_T - \chi') + \{(\chi_T - \chi_S)/2 \tan[(1+\alpha)\pi/2]\}^2]^{1/2} \tag{3}$$

The Arrhenius plots for **2** and **4** give straight lines indicating an Orbach (ORB) spin–lattice relaxation mechanism [eqn (4)]. However, experimental data for **1**, **3**, and **5** deviate from linearity at low temperatures and they tend to saturate (**3** and **5**) or really saturate (**1**) because of the aforementioned temperature-independent QTM [eqn (5)]. Hence, the QTM process is completely or partly suppressed after applying the dc field along this series of {$Fe^{III}_2 Ln^{III}_2$} squares, depending on the non-Kramer (Tb, Ho) or Kramer (Gd, Dy, Er) nature of the Ln^{III} ion, respectively. Satisfactory least-squares fits were obtained through the appropriate expressions derived from a single magnetic relaxation process via ORB mechanism (**2** and **4**) or a double magnetic relaxation process that combines ORB plus QTM (**1**, **3**, and **5**) mechanisms (solid lines in Fig. 5a).

$$\tau^{-1} = \tau_{ORB}^{-1} = \tau_0^{-1} \exp(-U_{eff}/k_B T) \tag{4}$$

This journal is © the Partner Organisations 2026

Inorg. Chem. Front., 2026, **13**, 3170–3185 | **3177**

$$\tau^{-1} = \tau_{\mathrm{QTM}}^{-1} \tag{5}$$

$$\tau^{-1} = \tau_{\mathrm{DIR}}^{-1} = AT \tag{6}$$

$$\tau^{-1} = \tau_{\mathrm{RAM}}^{-1} = CT^n \tag{7}$$

The resulting magnetic relaxation parameters of **1–5** are given in Table 3 and they are depicted in Fig. S28 in SI. The preexponential factor of the ORB process for **1–5** is within the range observed for other SMMs [τ_0 = 3 (**1**)/41 (**2**)/9.9 (**3**)/58 (**4**)/ 81 μs (**5**); Table 3] (Fig. S28b in SI). Notably, the effective energy barrier of the ORB process for the non-Kramer Tb(III) and Ho(III) derivatives **2** and **4** is one order of magnitude smaller than for the Kramer Dy(III) and Er(III) derivatives, **3** and **5** [U_{eff} = 0.92 (**2**)/8.8 (**3**)/0.78 (**4**)/3.81 cm^{-1} (**5**); Table 3] (Fig. S28c). Hence, an overall increase of the U_{eff} values occurs along this series in the order {Fe$_2^{\mathrm{III}}$Ho$_2^{\mathrm{III}}$} < {Fe$_2^{\mathrm{III}}$Tb$_2^{\mathrm{III}}$} < {Fe$_2^{\mathrm{III}}$Er$_2^{\mathrm{III}}$} < {Fe$_2^{\mathrm{III}}$Dy$_2^{\mathrm{III}}$}, while for the previously reported cyano-bridged {Fe$_2^{\mathrm{III}}$Ln$_2^{\mathrm{III}}$} squares analogues the Er(III) derivative had the largest value of U_{eff} [U_{eff} = 13–17 (Tb)/25–28 (Dy)/ 38–40 cm^{-1} (Er); Table S5].[59] The observed trend would be related to the different magnetic anisotropies of the {Fe$_2^{\mathrm{III}}$Ln$_2^{\mathrm{III}}$} ground state resulting from the antiparallel alignment of the spin and total momenta of the LS Fe$^{\mathrm{III}}$ and Ln$^{\mathrm{III}}$ ions [$J = 2(J_{\mathrm{Ln}} - S_{\mathrm{Fe}})$ = 11 (Tb), 14 (Dy), 15 (Ho), and 14 (Er)]. Otherwise, the U_{eff} value of 18 cm^{-1} for **1** is extremely large to be associated with a magnetic anisotropy energy barrier given the almost isotropic nature of the Gd$^{\mathrm{III}}$ ions (see discussion above). Slow-rate spin-phonon transitions between the vibronic energy levels of the {Fe$_2^{\mathrm{III}}$Gd$_2^{\mathrm{III}}$} square could be the source of the slower magnetic relaxation in **1**. Alternatively, the ln τ *vs.* ln T plots, which also give straight lines for **2** and **4** supporting a Raman (RAM) spin–lattice relaxation mechanism [eqn (7)]. Once again, the experimental data for **1**, **3**, and **5** deviate from linearity at low temperatures due to the aforementioned QTM and/or DIR mechanisms [eqn (5) and (6), respectively]. Satisfactory least-squares fits were thus obtained through the appropriate expressions derived from a single magnetic relaxation process

via RAM mechanism (**2** and **4**) or a multiple magnetic relaxation process that combines RAM plus QTM and DIR (**1**, **3**, and **5**) mechanisms (solid lines in Fig. 5b).

The Raman exponent for **2** and **4** is extremely low and not physically meaningful [n = 0.38 (**2**)/0.32 (**4**); Table 3], so that a Raman ($n \geq 2$) or even a direct (n = 1) process can be definitely discarded. Yet, the low n value for **1**, **3**, and **5** agree with a Raman process assisted by optical phonons [n = 3.9 (**1**)/2.8 (**3**)/ 3.6 (**5**); Table 3] (Fig. S28f in SI), as an alternative to the Orbach process discussed above. Indeed, satisfactory fits were also obtained by consider the simultaneous contributions of Raman, Orbach and QTM mechanisms for **1**, **3**, and **5**, with values of the respective magnetic relaxation parameters within the normal range for SMMs (see Table 3). However, their reliability is clearly limited by the large number of fitting parameters, which could lead to overparameterization. Otherwise, the coefficient factors of the DIR and RAM processes are within the range observed for other SMMs [A = 470 (**1**)/1020 (**3**)/660 s^{-1} K^{-1} (**5**) and C = 3 (**1**)/50 (**3**)/10 s^{-1} K^{-n} (**5**); Table 3], increasing in the order {Fe$_2^{\mathrm{III}}$Gd$_2^{\mathrm{III}}$} < {Fe$_2^{\mathrm{III}}$Er$_2^{\mathrm{III}}$} < {Fe$_2^{\mathrm{III}}$Dy$_2^{\mathrm{III}}$} along this series (Fig. S28d and S28e in SI). On the other hand, the relaxation times of the QTM process are similar regardless of the magnetic relaxation model employed, either ORB plus QTM [τ_{QTM} = 132 (**1**)/85 (**3**)/50 μs (**5**); Table 3] or RAM plus QTM and DIR [τ_{QTM} = 152 (**1**)/109 (**3**)/51 μs (**5**); Table 3], increasing in the order {Fe$_2^{\mathrm{III}}$Er$_2^{\mathrm{III}}$} < {Fe$_2^{\mathrm{III}}$Dy$_2^{\mathrm{III}}$} < {Fe$_2^{\mathrm{III}}$Gd$_2^{\mathrm{III}}$} along this series (Fig. S28a in SI).

Magnetocaloric properties

The magnetocaloric properties of **1–5** have been studied by variable-temperature (T = 2.0–10 K, with ΔT = 1 K) and variable-field (H = 0–5 T, with ΔH = 0.2 T) magnetization measurements to reveal the influence of the spin ground state and magnetic anisotropy of the Ln$^{\mathrm{III}}$ ion (Ln = Gd, Tb, Dy, Ho, and Er) on the magnetothermal behavior for this series of cyano-bridged heterometallic {Ln$_2^{\mathrm{III}}$Fe$_2^{\mathrm{III}}$} molecular squares as illustrative examples of 0D PBA (Table S6 in SI). Selected mag-

Table 3 Selected least-squares fitting parameters for the magnetic relaxation processes of **1–5**

	H (T)	$\tau_{\mathrm{QTM}}{}^a$ (μs)	$\tau_0{}^b$ (μs)	$U_{\mathrm{eff}}{}^b$ (cm^{-1})	A^c (s^{-1} K^{-1})	C^d (s^{-1} K^{-n})	n^d
1	1.0	132	3	18	—	—	—
		152	—	—	470	3	3.9
		126	3	16	—	0.04	3.4
2	0.5	—	41	0.92	—	—	—
		—	—	—	—	10 100	0.38
3	0.5	85	9.9	8.8	—	—	—
		109	—	—	1020	50	2.8
		109	61	3.3	—	33	2.8
4	0.5	—	58	0.4	—	—	—
		—	—	—	—	8200	0.32
5	0.5	50	81	3.8	—	—	—
		51	—	—	660	10	3.6
		94	95	0.05	—	58	2.7

^{a} Coefficient factor for the temperature-independent QTM process ($\tau^{-1} = \tau_{\mathrm{QTM}}^{-1}$). ^{b} Pre-exponential factor and effective energy barrier for the ORB process [$\tau^{-1} = \tau_0^{-1} \exp(-U_{\mathrm{eff}}/k_{\mathrm{B}}T)$]. ^{c} Coefficient factor for the DIR process ($\tau^{-1} = AT$). ^{d} Coefficient factor and exponent for the RAM process ($\tau^{-1} = CT^n$).

3178 | *Inorg. Chem. Front.*, 2026, **13**, 3170–3185

This journal is © the Partner Organisations 2026

Inorganic Chemistry Frontiers

Table 4 Selected magnetocaloric data for **1–5**

	H^a (T)	$T_{max}^{\ b}$ (K)	$-\Delta S_{max}^{\ c}$ (J kg^{-1} K^{-1})	T^d (K)	$H_{max}^{\ e}$ (T)	MCI^f (J kg^{-1} K^{-1} T^{-1})
1	5.0	<2.0	16.51	2.0	1.0	6.4
2	5.0	4.0	5.42	2.0	0.6	3.3
3	5.0	4.0	6.02	2.0	0.4	4.7
4	5.0	6.0	4.56	2.0	0.8	0.9
5	5.0	4.0	5.86	2.0	0.6	3.6

^{a} Magnetic field value. ^{b} Temperature value of the maximum of the magnetic entropy change. ^{c} Value of the maximum of the magnetic entropy change (in gravimetric units). ^{d} Temperature value. ^{e} Magnetic field value of the maximum of the magnetocaloric index. ^{f} Value of the maximum of the magnetocaloric index (in gravimetric units).
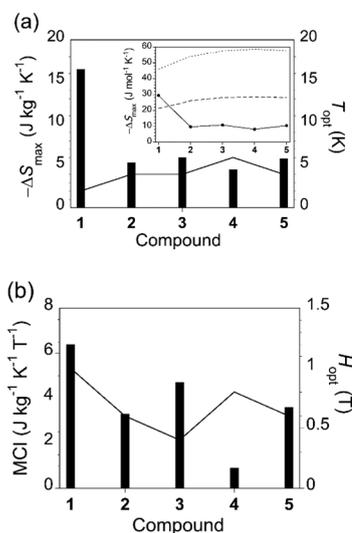
Fig. 6 Histogram plots showing the variation of the maximum values (in gravimetric units) of $-\Delta S_m$ (a) and MCI (b) for **1–5** (data from Table 4). The solid lines are the corresponding optimum values of the temperature and the magnetic field. The inset shows the maximum values (in molar units) of $-\Delta S_m$ (a) for **1–5**. The dotted and dashed lines correspond to the calculated values for two low-spin iron(III) and two lanthanide(III) ions, magnetically isolated or antiferromagnetically coupled, respectively, considering a negligible zero-field splitting (see text).

netocaloric data for **1–5** are summarized in Table 4 and they are depicted in Fig. 6.

The magnetic entropy change $(-\Delta S_m)$ after switching on the magnetic field $(\Delta H = H - H_0 = H$ with $H_0 = 0)$ can be estimated from the M vs. H and T plots (M being the gravimetric magnetization per $\{Ln_2^{III}Fe_2^{III}\}$ unit), according to the Maxwell equation.[81] The corresponding $-\Delta S_m$ vs. T and H color contour maps and plots for **1–5** are represented in Fig. 7a–e and Fig. S29 in SI, respectively.

Once again, the magnetothermal behavior of **2–5** are qualitatively similar, being different from that of **1**, as expected from the magnetically isotropic nature of the Gd^{III} ion compared to the other magnetically anisotropic Ln^{III} ions (Ln = Tb, Dy, Ho, and Er).

For **1**, the increase of magnetic field or the decrease of temperature determines a gradual increase of the magnetic entropy change for $T > 2$ K and $H < 5$ T (Fig. 7a, Fig. S29a and S29f in SI).

The maximum $-\Delta S_m$ value (in gravimetric units) is 16.51 J kg^{-1} K^{-1} at $T = 2$ K for $H = 5$ T (Table 4), being larger than that reported for the only other example of cyano-bridged $\{Fe^{III}(LS)_2Gd_2^{III}\}$ tetranuclear complex investigated to date as cryomagnetic refrigerant of formula $\{[Fe(htpzb)(CN)_2(\mu\text{-}CN)][Gd(H_4L)(H_2O)_2]\}_2\cdot 8H_2O\cdot 2CH_3OH$ [$H_6L = N,N'$-(2,6-pyridine-dicarboxyl)disalicylhydrazide] $(-\Delta S_{max} = 12.70$ J kg^{-1} K^{-1} at $T = 4.0$ K for $H = 7.0$ T; Table S6).[43] However, it is smaller than that reported for the related hydroxo/azido-bridged $\{Fe^{III}(HS)_3Gd_2^{III}\}$ pentanuclear complex of formula TBA$_3$[Fe$_3$Gd$_2$(N$_3$)$_{15}$(OH)$_3$(tipaH$_3$)$_2$] (TBA = tetrabutylammonium and tipaH$_3$ = triisopropanolamin) $(-\Delta S_{max} = 21.1$ J kg^{-1} K^{-1} at $T = 6.0$ K for $H = 7.0$ T).[42]

The maximum $-\Delta S_m$ value (in molar units) of 29.35 J mol^{-1} K^{-1} for **1** is smaller than the theoretical value for two LS Fe^{III} and two Gd^{III} ions, magnetically uncoupled [$-\Delta S_m = 2R\ln(2S_{Fe} + 1) + 2R\ln(2S_{Gd} + 1) = 5.55R = 45.89$ J mol^{-1} K^{-1}], being somewhat above than that of a tercet ground state [$S = 2(S_{Gd} - S_{Fe}) = 6$] resulting from the antiparallel alignment of the spin momenta of the LS Fe^{III} and Gd^{III} ions [$-\Delta S_m = R\ln(2S + 1) = 2.56R = 21.32$ J mol^{-1} K^{-1}]. This situation conforms to the partial thermal population of the low-lying states of higher multiplicity ($S > 6$) for the $\{Fe^{III}(LS)_2Gd_2^{III}\}$ complex, as expected for a relatively weak antiferromagnetic interaction between the LS Fe^{III} and two Gd^{III} ions through the cyanide bridges found in **1**.

Unlike **1**, the isofield curves of the magnetic entropy change for **2–5** develop a maximum with increasing the magnetic field for $H > 2.6$ (**2**), 3.0 (**3**), 1.0 (**4**), and 3.6 T (**5**) (Fig. S29b–e in SI), concomitantly with an intercrossing of the isothermal curves with decreasing the temperature for $T < 4.0$ (**2**), 3.0 (**3**), 5.0 (**4**), and 3.0 K (**5**) (Fig. S29g–j in SI). Hence, the maximum $-\Delta S_m$ values (in gravimetric units) are 5.42 (**2**), 6.02 (**3**), 4.56 (**4**), and 5.86 J kg^{-1} K^{-1} (**5**) at the optimum working temperatures $T_{opt} = T_{max} = 4.0$ (**2**), 4.0 (**3**), 6.0 (**4**), and 4.0 K (**5**) for $H = 5$ T (Table 4 and Fig. 6a). Interestingly, the maximum $-\Delta S_m$ values (in gravimetric units) for **1–5** are within the range observed earlier for mixed-3d/4f 0D PBA derivatives proposed as cryomagnetic refrigerants $(-\Delta S_{max} = 3.8$–17.7 J kg^{-1} K^{-1} at $T = 2$–8 K for $H = 7$ T; Table S6 in the SI).[82–84] Moreover, they are comparable to those reported for the lanthanide gallium garnets of general formula Ln$_3$Ga$_5$O$_{12}$ $[-\Delta S_{max} = 35.31$ (Gd), 11.22 (Tb), and 14.52 J kg^{-1} K^{-1} (Dy) at $T = 4$ (Gd), 3 (Tb), and 2 K (Dy) for $H = 3$ (Gd), 4 (Tb), and 2 T (Dy)].[85,86]

The maximum $-\Delta S_m$ values (in molar units) for **2–5** [$-\Delta S_{max} = 9.66$ (**2**), 10.77 (**3**), 8.14 (**4**), and 10.48 J mol^{-1} K^{-1} (**5**)] are significantly smaller than for **1** $(-\Delta S_{max} = 12.70$ J kg^{-1} K^{-1}) (inset of (Fig. 6a)). Overall, they vary in the order: **1** (Gd) $\gg$ **3** (Dy) $\approx$ **5** (Er) > **2** (Tb) > **4** (Ho), despite the increase of the total momentum almost in the inverse order: **4** ($J_{Ho} = 8$) > **3** = **5** ($J_{Dy} = J_{Er} = 15/2$) > **2** ($J_{Tb} = 6$) > **1** ($J_{Gd} = 7/2$). This situation is likely explained because of the increase of the local magnetic anisotropy from the Gd^{III} ion to the other Ln^{III} ions (Ln = Tb,

This journal is © the Partner Organisations 2026

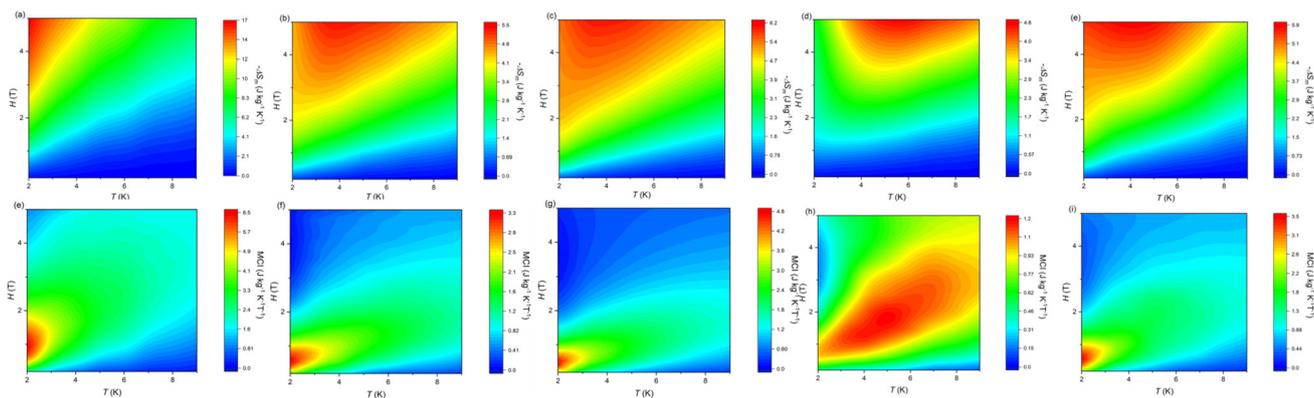Inorg. Chem. Front., 2026, **13**, 3170–3185 | **3179**

Fig. 7 Contour color map for the temperature and field dependence of the magnetic entropy change ($-\Delta S_m$) (a–e) and of the magnetocaloric efficiency index (MCI) (e–i), defined as $-\partial(\Delta S_m)/\partial H$ (in gravimetric units), after switching on the magnetic field for **1–5**, in the applied dc magnetic field and temperature ranges 2–10 K and 0–5 T, respectively.

Dy, Ho, and Er) along this series of cyano-bridged $\{Fe^{III}(LS)_2Ln^{III}\}$ complexes. Hence, the $-\Delta S_{max}$ values for **2–5** are almost five-fold lower than the ones calculated for two low-spin iron(III) and two lanthanide(III) ions, magnetically isolated, considering a negligible zero-field splitting $[-\Delta S_m = 2R\ln(2J_{Fe} + 1) + 2R\ln(2J_{Ln} + 1) = 54.17$ (**2**), 57.62 (**3**), 58.63 (**4**), and 56.72 J mol^{-1} K^{-1} (**5**)] (dotted line in the inset of Fig. 6a).

Otherwise, they are yet three-fold lower than those calculated for the ground state resulting from the antiparallel alignment of the total momenta of the LS Fe^{III} and Ln^{III} ions $[-\Delta S_m = R\ln(2J + 1) = 26.07$ (Tb), 28.00 (Dy), 28.55 (Ho), and 28.00 J mol^{-1} K^{-1} (Er) with $J = 2(J_{Ln} - J_{Fe}) = 11$ (Tb), 14 (Dy), 15 (Ho), and 14 (Er)] (dashed line in the inset of (Fig. 6a)). In fact, the large energy splitting of the ground state of the magnetically anisotropic Ln^{III} ions into their $\pm mJ$ levels strongly minimizes the magnetic entropy at zero field, thereby reducing the maximum magnetic entropy change after switching on the magnetic field.

On the other hand, the isothermal curves for **1**, **2**, **3**, and **5** rapidly increase monotonically, tending to saturate at lower temperatures (Fig. S29f–h and S29j in SI). In contrast, for **4**, the increase of the isothermal curves (Fig. S29i in SI) is more abrupt, the magnetic entropy change diverting at higher temperatures, while a slight tendency of saturation occurred at low temperatures (2 and 3 K). At low magnetic field, $H = 1$ T, the maximum value of the magnetic entropy change is 5.04 (**1**), 2.18 (**2**), 3.75 (**3**), 1.95 (**4**), and 2.94 J kg^{-1} K^{-1} (**5**) at 2 (**1**, **2**, **3**, **5**) and 4 K (**4**), representing 30 (**1**), 40 (**2**), 62 (**3**), 32 (**4**), and 50% (**5**) from the $-\Delta S_{max}$ value. This means that $-\Delta S_m$ are significant even at weak H comparable with ceramic (0.5–1 T) or Nd-based permanent magnets (1.4 T) and, also, are of interest in cryomagnetic refrigeration applications for which high $-\Delta S_{max}$ values and large slope of the field dependence of $-\Delta S_m$ plots are required.

In this respect, it is convenient to introduce the magnetocaloric efficiency index (MCI) as a new figure of merit for cryomagnetic refrigerants, defined as MCI $= -\partial(\Delta S_m)/\partial H$, which corresponds precisely to $-\partial M/\partial T$ according to the Maxwell equation $[-\Delta S_m = \int (\partial M/\partial T)dH]$.[87] Hence, the isofield and isothermal curves for **1–5** develop narrow to broad maxima of MCI which

shift toward higher temperatures or fields with increasing the field or the temperature, respectively (Fig. 7e–i and Fig. S30 in SI). These MCI maxima cover a broad (**1**) to narrow (**2–5**) field range $[H_{max} = 1.0$–3.8 (**1**)/0.6–1.8 (**2**)/0.4–1.6 (**3**)/0.8–2.8 (**4**)/0.6–2.2 T (**5**) for $T = 2$–10 K] (Fig. S30f–j in SI), so that the lowest optimum working field $[H_{opt} = H_{max} = 1.0$ (**1**)/0.6 (**2**)/0.4 (**3**)/0.8 (**4**)/0.6 T (**5**) at $T = 2$ K; Table 4] along this family of cyano-bridged $\{Fe^{III}(LS)_2Ln_2^{III}\}$ molecular squares decrease in the order: **1** (Gd) > **4** (Ho) > **2** (Tb) = **5** (Er) > **3** (Dy). The intensity and the location of these MCI maxima in the low-field region are both mandatory for the practical applications of mixed-3d/4f 0D PBA derivatives as magnetic refrigerants at low temperatures, just above the He liquefaction temperature.

Hence, the MCI performance for **1** is rather high at the optimum working field (MCI = 6.4 J kg^{-1} K^{-1} T^{-1} for $H_{opt} = 1.0$ T at $T = 2$ K; Table 4). However, high to moderate MCI performances can be obtained using smaller optimum working fields for **2–5** [MCI = 3.3 (**2**), 4.7 (**3**), 0.9 (**4**), and 3.6 J kg^{-1} K^{-1} T^{-1} (**5**) for $H_{opt} = H_{max} = 0.6$ (**2**), 0.4 (**3**), 0.8 (**4**), and 0.6 T (**5**) at $T = 2$ K; Table 4 and Fig. 6b], approaching the H values of the permanent magnets used commercially (ranging from 0.15 and 2 T for Alnico, a common refrigerator magnet). In this family of cyano-bridged $\{Fe^{III}(LS)_2Ln_2^{III}\}$ molecular squares, a decrease of the MCI performance at the optimal working field is found with increasing the magnetic anisotropy in the order: **1** (Gd) > **3** (Dy) > **5** (Er) $\approx$ **2** (Tb) > **4** (Ho), so that it decreases approximately with increasing the J value in the order: **1** $(J_{Gd} = 7/2)$ < **2** $(J_{Tb} = 6)$ < **3** = **5** $(J_{Dy} = J_{Er} = 15/2)$ < **4** $(J_{Ho} = 8)$. Otherwise, the corresponding lanthanide gallium garnets Ln$_3$Ga$_5$O$_{12}$ show similar MCE performances than **1–5**, but at higher optimum working fields [MCI = 8.47 (Gd), 4.90 (Tb), and 6.84 J kg^{-1} K^{-1} (Dy), at $T = 4$ K for $H_{opt} = 2$ (Gd), 1 (Tb), and 1 T (Dy)].[87]

Conclusions

A new isostructural series of cyano-bridged mixed-3d/4f square-shaped tetranuclear complexes was obtained through

3180 | *Inorg. Chem. Front.*, 2026, **13**, 3170–3185

This journal is © the Partner Organisations 2026

the "complex-as-ligand/complex-as-metal" strategy by employing heteroleptic iron(III) tricyanometallates with the scorpionate-like hydrotris(pyrazolyl)borate ligand (htpzb) that acts as angular connector toward coordinatively unsaturated lanthanide(III) complexes capped with chelating 4,4′-dimethyl-2,2′-bipyridine (dmbpy) and nitrate ligands.

These antiferromagnetically coupled $\{Fe^{III}_2Ln^{III}_2\}$ squares (Ln = Gd, Tb, Dy, Ho, and Er) constitute a unique class of field-induced single-molecule magnets (SMMs). Remarkably, $\{Fe^{III}_2Gd^{III}_2\}$ is a rare example of quasi-isotropic gadolinium (III)-containing SMM that exhibit slow magnetic relaxation (SMR) under a low applied field ($H = 1.0$ T) at relatively high blocking temperatures (T_B up to 6.0 K). The orbital contribution of the other lanthanides(III) gives rise to significant magnetic anisotropy that, together with their large magnetic moments, provide the main "ingredients" for the assembly of SMMs. The SMR properties of the resulting $\{Fe^{III}_2Ln^{III}_2\}$ squares occurred, however, at lower blocking temperatures ($T_B < 4.0$ K) under a lower applied field ($H = 0.5$ T), being very sensitive to the nature of the magnetically anisotropic Ln^{III} ions (Ln = Tb, Dy, Ho, and Er). Besides, the octahedral low-spin (LS) iron(III) building block with first order orbital moment has a pronounced molecular easy axis of magnetization, being well-suited for the assembly of mixed-3d–4f SMMs.

The magneto-thermal properties along this series of $\{Fe^{III}_2Ln^{III}_2\}$ squares also depends on the magnetic anisotropy of the Ln^{III} ions (Ln = Gd, Tb, Dy, Ho, and Er), the large magnetocaloric efficiency being found for the magnetically isotropic $\{Fe^{III}_2Gd^{III}_2\}$ square at optimal working temperature and field of 2.0 K and 1.0 T, respectively, while the magnetically anisotropic $\{Fe^{III}_2Ln^{III}_2\}$ squares (Ln = Tb, Dy, Ho, and Er) showed moderate to high magnetocaloric efficiencies at higher optimum working temperatures ($T_{opt} = 4.0$–6.0 K) and lower optimum working fields ($H_{opt} = 0.4$–1.0 T). This new family of cyano-based mixed-3d/4f SMMs belonging to the large class of zero-dimensional (0D) lanthanide Prussian blue analogues (Ln PBA) then emerges as a new route toward molecular magnetic coolers operating just above the helium liquefaction temperature. Therefore, the perspectives of exploration MCE in high-dimensional (2D and 3D) lanthanide PBA are wide and promising and could provide very interesting multifunctional molecular materials that advance the knowledge in magnetochemistry and, also, of relevance in adiabatic demagnetization refrigeration (ADR).

Conflicts of interest

There are no conflicts to declare.

Data availability

The authors declare that the data supporting this article have been included as part of the supplementary information (SI).

Supplementary information: FTIR spectra (Fig. S1–S5, **1–5**); UV-Vis spectra for **1–5** (Fig. S6); PXRD patterns (Fig. S7–S11, **1–5**); square-like units and Fe^{III}/Ln^{III} coordination polyhedra (Fig. S12–S15, **2–5**); drawings of the crystal packing for **2–5** (Fig. S16–S23, **2–5**); crystallographic data (Tables S1 and S2, **1–5**), SHAPE analysis (Table S3, **1–5**) and H-bond parameters (Table S4, **1–5**), dc and ac magnetic parameters for cyano-bridged $\{Ln^{III}_2Fe^{III}_2\}$ squares (Table S5); dc plots of M vs. HT^{-1} for **1–5** (Fig. S24); ac plots of χ' and χ'' vs. ν for **1–5** (Fig. S25); Cole–Cole plots for **1–5** (Fig. S26); temperature dependence of χ_T, χ_S, and α parameters plots for **1–5** (Fig. S27); plots showing the variation of the values of τ_{QTM} (a), τ_0 (b), and U_{eff} (c), A (d), C (e), and n (f) for the QTM, and ORB, DIR, and RAM relaxation mechanisms in **1–5** series (Fig. S28); selected magnetocaloric data for mixed-3d/nd 0D PBAs proposed as cryomagnetic refrigerants (Table S6); temperature and field dependence of $-\Delta S_m$ (Fig. S29) and of MCI plots, respectively (Fig. S30) for **1–5**. See DOI: https://doi.org/10.1039/d5qi02520f.

CCDC 2504399–2504403 contain the supplementary crystallographic data for this paper.[88a–e]

References

1 T. Mwanza, G. S. Kürkçüoğlu, H. Ünver, O. Şahin and O. Yeşilel, Synthesis, spectroscopic, structural characterizations, and catalytic properties of cyanide-bridged heteronuclear metal organic frameworks with imidazole, *J. Solid State Chem.*, 2022, **314**, 123344.

2 A. Fonseca, A. L. Bugaev, A. Y. Pnevskaya, K. Janssens, C. Marquez and D. De Vos, Copper-cobalt double metal cyanides as green catalysts for phosphoramidate synthesis, *Commun. Chem.*, 2023, **6**, 141.

3 Z. Song, B. Subramaniam and R. V. Chaudhari, Transesterification of Propylene Carbonate with Methanol Using Fe–Mn Double Metal Cyanide Catalyst, *Chem. Eng.*, 2019, **7**, 5698.

4 K. Y. Cohen, A. Reinhold, R. Evans, T. S. Lee, H.-Y. Kuo, D. G. Nedd, G. D. Scholes and A. B. Bocarsly, Elucidating

This journal is © the Partner Organisations 2026

Inorg. Chem. Front., 2026, **13**, 3170–3185 | **3181**

the mechanism of photochemical CO_2 reduction to CO using a cyanide-bridged di-manganese complex, *Dalton Trans.*, 2022, **51**, 17203.

5 K. Y. Cohen, R. Evans, S. Dulovic and A. B. Bocarsly, Using Light and Electrons to Bend Carbon Dioxide: Developing and Understanding Catalysts for CO_2 Conversion to Fuels and Feedstocks, *Acc. Chem. Res.*, 2022, **55**, 944.

6 B. Zakrzewska, A. Jabłońska, L. Adamczyk, B. Dembińska, A. Kostuch, M. Strawski, I. A. Rutkowska, P. J. Kulesza, M. Marcinek, J. A. Cox and K. Miecznikowski, Pyrolyzed cobalt hexacyanocobaltate dispersed on reduced-graphene-oxide as an electrocatalyst of the oxygen reduction reaction in an alkaline medium, *J. Mater. Chem. A*, 2023, **11**, 7286.

7 M. J. Murphy, K. A. Zenere, F. Ragon, P. D. Southon, C. J. Keper and S. M. Neville, Guest Programmable Multistep Spin Crossover in a Porous 2-D Hofmann-Type Material, *J. Am. Chem. Soc.*, 2017, **139**, 1330.

8 J. Liu, M. Zheng, S. Wuc and L. Zhang, Design strategies for coordination polymers as electrodes and electrolytes in rechargeable lithium batteries, *Coord. Chem. Rev.*, 2023, **483**, 215084.

9 J.-R. Jiménez, A. Sugahara, M. Okubo, A. Yamada, L.-M. Chamoreau, L. Lisnardand and R. Lescouëzec, A $[Fe^{III}(Tp)(CN)_3]^-$ scorpionate-based complex as a building block for designing ion storage hosts (Tp: hydrotrispyrazolylborate), *Chem. Commun.*, 2018, **54**, 5189.

10 J. J. Zakrzewski, M. Liberka, M. Zychowicz and S. Chorazy, Diverse physical functionalities of rare-earth hexacyanidometallate frameworks and their molecular analogues, *Inorg. Chem. Front.*, 2021, **8**, 452.

11 R. Jankowski, M. Wyczesany and S. Chorazy, Multifunctionality of luminescent molecular nanomagnets based on lanthanide complexes, *Chem. Commun.*, 2023, **59**, 5961.

12 J.-T. Chen, T.-D. Zhou and W.-B. Sun, Multifunctional lanthanide-based single-molecule magnets exhibiting luminescence thermometry and photochromic and ferroelectric properties, *Dalton Trans.*, 2023, **52**, 4643.

13 D. Aguilà, Y. Prado, E. S. Koumousi, C. Mathonière and R. Clérac, Multifunctional lanthanide-based single-molecule magnets exhibiting luminescence thermometry and photochromic and ferroelectric properties, *Chem. Soc. Rev.*, 2016, **45**, 203.

14 J.-H. Wang, Z.-Y. Li, M. Yamashita and X.-H. Bu, Switchable Fe/Co Prussian blue networks and molecular analogues, *Coord. Chem. Rev.*, 2021, **428**, 23617.

15 C. E. Plecnik, S. Liu and S. G. Shore, Recent progress on cyano-bridged transition-metal-based single-molecule magnets and single-chain magnets, *Acc. Chem. Res.*, 2003, **36**, 499.

16 Y.-G. Huang, F.-L. Jiang and M.-C. Hong, Magnetic lanthanide–transition-metal organic–inorganic hybrid materials: From discrete clusters to extended frameworks, *Coord. Chem. Rev.*, 2009, **253**, 2814.

17 S. Zhang and P. Cheng, Recent advances in the construction of lanthanide-copper heterometallic metal-organic frameworks, *CrystEngComm*, 2015, **17**, 4250.

18 M. Ferbinteanu, F. Cimpoesu and S. Tanase, Metal-organic frameworks with d-f cyanide bridges: structural diversity, bonding regime, and magnetism, *Struct. Bonding*, 2015, **163**, 185.

19 W. Shi, K. Liu and P. Cheng, Transition-lanthanide hetero-metal-organic frameworks: synthesis, structures, and properties, *Struct. Bonding*, 2015, **163**, 231.

20 A. Dey, P. Bag, P. Kalita and V. Chandrasekhar, Heterometallic Cu^{II}–Ln^{III} complexes: Single molecule magnets and magnetic refrigerants, *Coord. Chem. Rev.*, 2021, **432**, 213707.

21 J. Wang, C.-Y. Sun, Q. Zheng, D.-Q. Wang, Y.-T. Chen, J.-F. Ju, T.-M. Sun, Y. Cui, Y. Ding and Y.-F. Tang, Lanthanide Single-Molecule Magnets: Synthetic Strategy, Structures, Properties and Recent Advances, *Chem. – Asian J.*, 2023, **18**, e202201297.

22 R. Marin, G. Brunet and M. Murugesu, Shining New Light on Multifunctional Lanthanide Single-Molecule Magnets, *Angew. Chem., Int. Ed.*, 2021, **60**, 1728.

23 K.-Q. Hu, X. Jiang, S.-Q. Wu, C.-M. Liu, A.-L. Cui and H.-Z. Kou, Slow Magnetization Relaxation in $Ni^{II}Dy^{III}Fe^{III}$ Molecular Cycles, *Inorg. Chem.*, 2015, **54**, 1206.

24 H. Weihe, J. Bendix, F. Tuna and S. Piligkos, Toward Molecular 4f Single-Ion Magnet Qubits, *J. Am. Chem. Soc.*, 2016, **138**, 5801.

25 M. Shiddiq, D. Komijani, Y. Duan, A. Gaita-Ariño, E. Coronado and S. Hill, Enhancing Coherence in Molecular Spin Qubits via Atomic Clock Transitions, *Nature*, 2016, **531**, 348.

26 X.-Y. Zheng, X.-J. Kong, Z. Zheng, L.-S. Long and L.-S. Zheng, High-Nuclearity Lanthanide-Containing Clusters as Potential Molecular Magnetic Coolers, *Acc. Chem. Res.*, 2018, **51**, 517.

27 Y. Yang, Y.-X. Wang, Y.-Z. Leia and P. Cheng, Asymmetric triply bridged lanthanide binuclear clusters with distinctly different magnetic behaviors, *Dalton Trans.*, 2024, **53**, 19097.

28 M. Orts-Arroyo, R. Rabelo, A. Carrasco-Berlanga, N. Moliner, J. Cano, M. Julve, F. Lloret, G. De Munno, R. Ruiz-García, J. Mayans, J. Martínez-Lillo and I. Castro, Field-induced slow magnetic relaxation and magnetocaloric effects in an oxalato-bridged gadolinium(III)-based 2D MOF, *Dalton Trans.*, 2021, **50**, 3801.

29 A. Mondal, M. Raizada, P. K. Sahu and S. Konar, A new family of Fe_4Ln_4 (Ln = Dy^{III}, Gd^{III}, Y^{III}) wheel type complexes with ferromagnetic interaction, magnetocaloric effect and zero-field SMM behavior, *Inorg. Chem. Front.*, 2021, **8**, 4625.

30 G. Lorusso, O. Roubeau and M. Evangelisti, Rotating Magnetocaloric Effect in an Anisotropic Molecular Dimer, *Angew. Chem., Int. Ed.*, 2016, **55**, 3360.

31 P. Konieczny, D. Czernia and T. Kajiwara, Rotating magnetocaloric effect in highly anisotropic Tb^{III} and Dy^{III} single molecular magnets, *Sci. Rep.*, 2022, **1216**, 601.

32 Y.-S. Ding and Y.-Z. Zheng, Anisotropic magnetocaloric effect in a dysprosium(III) single-molecule magnet.

3182 | *Inorg. Chem. Front.*, 2026, **13**, 3170–3185

This journal is © the Partner Organisations 2026

Commemorating the 100th anniversary of the birth of Academician Guangxian Xu, *J. Rare Earths*, 2021, **39**, 1554.

33 L. Tacconi, A. S. Manvell, M. Briganti, D. Czernia, H. Weihe, P. Konieczny, J. Bendix and M. Perfetti, Exploiting High Order Magnetic Anisotropy for Advanced Magnetocaloric Refrigerants, *Angew. Chem., Int. Ed.*, 2025, **64**, e202417582.

34 B. Rodríguez-Barea, J. Mayans, R. Rabelo, A. Sanchis-Perucho, N. Moliner, J. Martínez-Lillo, M. Julve, F. Lloret, R. Ruiz-García and J. Cano, Holmium(III) Single-Ion Magnet for Cryomagnetic Refrigeration Based on an MRI Contrast Agent Derivative, *Inorg. Chem.*, 2021, **60**, 12719.

35 N. El Alouani Dahmouni, M. Orts-Arroyo, A. Sanchis-Perucho, N. Moliner, J. Mayans, M. Pacheco, I. Castro, G. De Munno, N. Marino, R. Ruíz-García and J. Martínez-Lillo, Magnetocaloric efficiency tuning through solvent-triggered 3D to 2D interconversion in holmium(III)-based dynamic MOFs, *Chem. Commun.*, 2024, **60**, 7451.

36 P. J. Saines, J. A. M. Paddison, P. M. M. Thygesen and M. G. Tucker, Searching beyond Gd for magnetocaloric frameworks: magnetic properties and interactions of the $Ln(HCO_2)_3$ series, *Mater. Horiz.*, 2015, **2**, 528.

37 J. W. Maciel, L. H. G. Kalinke, R. Rabelo, M. E. Alvarenga, F. T. Martins, N. Moliner and D. Cangussu, Slow Relaxation of Magnetization and Magnetocaloric Effects in One-Dimensional Oxamato-Based Lanthanide(III) Coordination Polymers, *Magnetochemistry*, 2025, **11**, 23.

38 Z. Li, A. Arauzo, J. G. Planas and E. Bartolomé, Magnetic properties and magnetocaloric effect of Ln = Dy, Tb carborane-based metal–organic frameworks, *Dalton Trans.*, 2024, **53**, 8969–8979.

39 Z. Li, A. Arauzo, C. Roscini, J. G. Planas and E. Bartolomé, Multifunctional self-refrigerated multivariate {GdLn} (Ln = Dy, Tb, Tb/Eu) metal–organic frameworks, *J. Mater. Chem. A*, 2024, **12**, 21971.

40 J.-L. Liu, Y.-C. Chen, F.-S. Guo and M.-L. Tong, Recent advances in the design of magnetic molecules for use as cryogenic magnetic coolants, *Coord. Chem. Rev.*, 2014, **281**, 26–49.

41 P. Konieczny, W. Sas, D. Czernia, A. Pacanowsk, M. Fitta and R. Pełka, Magnetic cooling: a molecular perspective, *Dalton Trans.*, 2022, **51**, 12762–12780.

42 S. F. M. Schmidt, M. P. Merkel, G. E. Kostakis, G. Buth, C. E. Ansona and A. K. Powell, SMM behaviour and magnetocaloric effect in heterometallic 3d–4f coordination clusters with high azide: metal ratios, *Dalton Trans.*, 2017, **46**, 15661.

43 L.-Z. Cai, W. Zhang, Z.-X. Zhu, J. Ru and M.-X. Yao, Synthesis, structures and magnetic properties of cyano- and amide-bridged Fe^{III}-Ln^{III} tetranuclear heterometallic clusters, *J. Coord. Chem.*, 2019, **72**, 1097.

44 R. Lescouëzec, L. M. Toma, J. Vaissermann, M. Verdaguer, F. S. Delgado, C. Ruiz-Pérez, F. Lloret and M. Julve, Design of single chain magnets through cyanide-bearing six-coordinate complexes, *Coord. Chem. Rev.*, 2005, **249**, 2691.

45 L. M. Toma, L. D. Toma, F. S. Delgado, C. Ruiz-Pérez, J. Sletten, J. Cano, J. M. Clemente-Juan, F. Lloret and M. Julve, Trans-dicyanobis(acetylacetonato)ruthenate(III) as a precursor to build novel cyanide-bridged Ru^{III}–M^{II} bimetallic compounds [M = Co and Ni], *Coord. Chem. Rev.*, 2006, **250**, 2176.

46 S. Wang, X.-H. Ding, Y.-H. Li and W. Huang, Dicyanometalate chemistry: A type of versatile building block for the construction of cyanide-bridged molecular architectures, *Coord. Chem. Rev.*, 2012, **256**, 439.

47 Y.-H. Li, W.-R. He, X.-H. Ding, S. Wang, L.-F. Cui and W. Huang, Cyanide-bridged assemblies constructed from capped tetracyanometalate building blocks $[M_A(ligand)(CN)_4]^{1-/2-}$ (M_A = Fe or Cr), *Coord. Chem. Rev.*, 2012, **256**, 2795.

48 S. Wang, X.-H. Ding, J.-L. Zuo, X.-Z. You and W. Huang, Tricyanometalate molecular chemistry: A type of versatile building blocks for the construction of cyano-bridged molecular architectures, *Coord. Chem. Rev.*, 2011, **255**, 1713.

49 T. Shiga, N. Mihara and M. Nihei, Cyanide-bridged assemblies with tricyanometalates, *Coord. Chem. Rev.*, 2022, **472**, 214763.

50 M. Andruh, Heterotrimetallic complexes in molecular magnetism, *Chem. Commun.*, 2018, **54**, 3559.

51 M.-G. Alexandru, D. Visinescu, S. Shova, M. Andruh, F. Lloret and M. Julve, Crystal Structures, and Magnetic Properties of Two Novel Cyanido-Bridged Heterotrimetallic {$Cu^{II}Mn^{II}Cr^{III}$} Complexes, *Inorg. Chem.*, 2017, **56**, 2258.

52 D. Visinescu, O. Fabelo, C. Ruiz-Perez, F. Lloret and M. Julve, Synthesis, $[Fe(phen)(CN)_4]^-$: a suitable metalloligand unit to build 3d–4f heterobimetallic complexes with mixed bpym-cyano bridges (phen = 1,10-phenantroline, bpym = 2,2′-bipyrimidine), *CrystEngComm*, 2010, **12**, 2454.

53 X.-J. Song, J.-J. Xu, Y. Chen, M. Muddassir, F. Cao, R.-M. Wei, Y. Song and X.-Z. You, Synthesis, structures and magnetic properties of cyano-bridged 3d–4f rectangular tetranuclear [$Fe^{III}_2Ln^{III}_2$] (Ln = Y, Tb, Dy) compounds containing [$Fe^{III}(bpy)(CN)_4$]$^-$ unit, *Polyhedron*, 2013, **66**, 212.

54 M.-G. Alexandru, D. Visinescu, M. Andruh, N. Marino, D. Armentano, J. Cano, F. Lloret and M. Julve, Heterotrimetallic Coordination Polymers: {$Cu^{II}Ln^{III}Fe^{III}$} Chains and {$Ni^{II}Ln^{III}Fe^{III}$} Layers: Synthesis, Crystal Structures, and Magnetic Properties, *Chem. – Eur. J.*, 2015, **21**, 5429.

55 D. Visinescu, M.-G. Alexandru, D. G. Dumitrescu, S. Shova, N. Moliner, F. Lloret and M. Julve, Cyanido-bridged {$Fe^{III}Ln^{III}$} heterobimetallic chains assembled through the [Fe^{III}{$HB(pz)_3$}$(CN)_3$]$^-$ complex as metalloligand: synthesis, crystal structure and magnetic properties, *CrystEngComm*, 2021, **23**, 4615.

56 D. Visinescu, L. M. Toma, O. Fabelo, C. Ruiz-Pérez, F. Lloret and M. Julve, Low-Dimensional 3d–4f Complexes Assembled, by Low-Spin [$Fe^{III}(phen)(CN)_4$]$^-$ Anions, *Inorg. Chem.*, 2013, **52**, 1525.

57 M.-G. Alexandru, D. Visinescu, S. Shova, W. X. C. Oliveira, F. Lloret and M. Julve, Design of 3d–4f molecular squares through the [Fe{$(HB(pz)_3$}$(CN)_3$]$^-$ metalloligand, *Dalton Trans.*, 2018, **47**, 6005.

This journal is © the Partner Organisations 2026

Inorg. Chem. Front., 2026, **13**, 3170–3185 | **3183**

58 M.-G. Alexandru, D. Visinescu, B. Braun-Cula, S. Shova, F. Lloret and M. Julve, In situ generation of Ph₃PO in cyanido-bridged heterometallic {Fe^III Ln^III}₂ molecular squares (Ln = Eu, Sm), *Dalton Trans.*, 2019, **48**, 7532.

59 M.-G. Alexandru, D. Visinescu, B. Cula, S. Shova, R. Rabelo, N. Moliner, F. Lloret, J. Cano and M. Julve, A rare isostructural series of 3d–4f cyanido-bridged heterometallic squares obtained by assembling [Fe^III{HB(pz)₃}(CN)₃]⁻ and Ln^III ions: synthesis, X-ray structure and cryomagnetic study, *Dalton Trans.*, 2021, **50**, 14640.

60 M.-G. Alexandru, D. Visinescu, J. Cano, F. Lloret and M. Julve, Cyanido-Bridged Heterobimetallic Molecular Squares: Low-Dimensional Models of Prussian Blue Analogues and Beyond, *Cryst. Growth Des.*, 2023, **23**, 1288.

61 Y.-F. Huang, H.-H. Wei and M. Katada, A cyano-bridged hetero-tetranuclear [Sm₂(o-phen)₂(DMF)₆(H₂O)₂((-CN)₄Fe₂(CN)₈]·5H₂O·CH₃OH: synthesis, structure, Mössbauer spectrum, and magnetism, *J. Coord. Chem.*, 2008, **61**, 2683.

62 H. Zhou, D.-Y. Yu, H.-B. Zhou and A.-H. Yuan, Cyanide-Bridged Tetranuclear RE^III₂Fe^III₂ (RE = Y, Tb, Dy) Molecular Squares with 2,2′:6′,2″-Terpyridine as a Capping Ligand, *Z. Anorg. Allg. Chem.*, 2015, **641**, 858.

63 M. Muddassir, X.-J. Song, Y. Chen, F. Cao, R.-M. Wei and Y. Song, Ion-induced diversity in structure and magnetic properties of hexacyanometalate–lanthanide bimetallic assemblies, *CrystEngComm*, 2013, **15**, 10541.

64 Z.-G. Gu, W. Liu, Q.-F. Yang, X.-H. Zhou, J.-L. Zuo and X.-Z. You, Cyano-Bridged Fe^III₂Cu^II₃ and Fe^III₄Ni^II₄ Complexes: Syntheses, Structures, and Magnetic Properties, *Inorg. Chem.*, 2007, **46**, 3236.

65 Rigaku Oxford Diffraction, *CrysAlis Pro Software System*, Rigaku Corporation, Oxford, UK, 2015; CrysAlis Pro v. 1.171.38.46.

66 G. M. Sheldrick, SHELXT—Integrated Space-Group and Crystal-Structure Determination, *Acta Crystallogr., Sect. A: Found. Crystallogr.*, 2015, **71**, 3.

67 G. M. Sheldrick, Crystal Structure Refinement with SHELXL, *Acta Crystallogr., Sect. C: Struct. Chem.*, 2015, **71**, 3.

68 O. Dolman, L. J. Bourhis, R. J. Gildea, J. A. K. Howard and H. Puschmann, OLEX2: A Complete Structure Solution, Refinement and Analysis Program, *J. Appl. Crystallogr.*, 2009, **42**, 339.

69 H. Putz and K. Brandenburg, *Diamond—Crystal and Molecular Structure Visualization*, Crystal Impact, Bonn, Germany. Available online: **https://www.crystalimpact.com/diamond**.

70 M. R. Rosenthal, The myth of the non-coordinating anion, *J. Chem. Educ.*, 1973, **50**, 331.

71 Y. Ye, P. Garrido-Barros, J. Wellauer, C. M. Cruz, R. Lescouëzec, O. S. Wenger, J. M. Herrera and J.-R. Jiménez, Luminescence and Excited-State Reactivity in a Heteroleptic Tricyanido Fe(III) Complex, *J. Am. Chem. Soc.*, 2024, **146**, 954.

72 M. Llunell, D. Casanova, J. Cirera, J. M. Bofill, P. Alemany, S. Alvarez, M. Pinsky and D. Avnir, *SHAPE: Continuous shape measures of polygonal and polyhedral molecular fragments, 1.1b*, University of Barcelona, Barcelona, 2005.

73 D. Casanova, M. Llunell, P. Alemany and S. Alvarez, The Rich Stereochemistry of Eight-Vertex Polyhedra: A Continuous Shape Measures Study, *Chem. – Eur. J.*, 2005, **11**, 1479.

74 R. Lescouëzec, J. Vaissermann, F. Lloret, M. Julve and M. Verdaguer, Ferromagnetic Coupling between Low- and High-Spin Iron(III) Ions in the Tetranuclear Complex fac-{[Fe^III{HB(pz)₃}(CN)₂(μ-CN)]₃Fe^III(H₂O)₃}·6H₂O ([HB(pz)₃]⁻ = Hydrotris(1-pyrazolyl)borate), *Inorg. Chem.*, 2002, **41**, 5943.

75 Q.-P. Qin, Z.-F. Wang, M.-X. Tan, X.-L. Huang, H.-H. Zou, B.-Q. Zou, B.-B. Shi and S.-H. Zhang, Complexes of lanthanides(III) with mixed 2,2′-bipyridyl and 5,7-dibromo-8-quinolinoline chelating ligands as a new class of promising anti-cancer agents, *Metallomics*, 2019, **11**, 1005.

76 F. A. Mautner, F. Bierbaumer, R. C. Fischer, A. Torvisco, R. Vicente, M. Font-Bardía, À. Tubau, S. Speed and S. S. Massoud, Diverse Coordination Numbers and Geometries in Pyridyl Adducts of Lanthanide(III) Complexes Based on β-Diketonate, *Inorganics*, 2021, **9**, 74.

77 E. C. Queiroz, C. H. J. Franco, M. S. Ferreira, R. O. Freire and F. C. Machado, Photoluminescent complexes of Eu(III), Tb(III) and Gd(III) with 3-thiopheneacetate and 4,4′-dimethyl-2,2′-bipyridine: Synthesis, characterization and photophysical properties, *J. Lumin.*, 2022, **249**, 118990.

78 P. Hu, F.-P. Xiao, Y. Li, J.-F. Cao, Z.-S. Chen, L.-L. Zhu and W.-P. Huang, One mononuclear single-molecule magnet derived from Dy(III) and dmbpy (dmbpy = 4,4′-dimethyl-2,2′-dipyridyl), *Inorg. Chem. Commun.*, 2017, **84**, 207.

79 K. P. Zhuravlev, V. I. Tsaryuka, A. V. Vologzhanina, P. V. Dorovatovskii, Y. V. Zubavichus, V. A. Kudryashova and Z. S. Klemenkova, Structural peculiarities and luminescence of europium dipivaloylmethanates with 2,2′-bipyridine derivatives. Polymorphism of [Eu(DPM)₃Bpy], *Inorg. Chim. Acta*, 2020, **502**, 119294.

80 K. S. Cole and R. H. Cole, Dispersion and Absorption in Dielectrics. I. Alternating Current Characteristics, *J. Chem. Phys.*, 1941, **9**, 341–351.

81 L. Tocado, E. Palacios and R. Burriel, Entropy determinations and magnetocaloric parameters in systems with first order transitions: Study of MnAs, *J. Appl. Phys.*, 2009, **105**, 093918.

82 M. Gajewski, R. Pełka, M. Fitta, Y. Miyazaki, Y. Nakazawa, M. Bałanda, M. Reczynski, B. Nowicka and B. Sieklucka, Magnetocaloric effect of high spin cluster with Ni₉W₆ core, *J. Magn. Magn. Mater.*, 2016, **414**, 25.

83 M. Arczynski, M. Rams, J. Stanek, M. Fitta, B. Sieklucka, K. R. Dunbar and D. Pinkowicz, A Family of Octahedral Magnetic Molecules Based on [Nb^IV(CN)₈]⁴⁻, *Inorg. Chem.*, 2017, **56**, 4021.

84 W. Wen, Y.-S. Meng, C.-Q. Jiao, Q. Liu, H.-L. Zhu, Y.-M. Li, H. Oshio and T. Liu, Ferromagnetic Archimedean polyhedra {Fe₂₄M₁₈} (M = Fe, Ni, and Mn) with tunable electron configurations, *Inorg. Chem. Front.*, 2021, **8**, 4239.

3184 | *Inorg. Chem. Front.*, 2026, **13**, 3170–3185

This journal is © the Partner Organisations 2026

85 B. Daudin, R. Lagnier and B. Salce, Thermodynamic Properties of the Gadolinium Gallium Garnet, $Gd_3Ga_5O_{12}$, between 0.05 and 25 K, *J. Magn. Magn. Mater.*, 1982, **27**, 315.

86 M. Kleinhans, K. Eibensteiner, J. C. Leiner, C. Resch, L. Worch, M. A. Wilde, J. Spallek, A. Regnat and C. Pfleiderer, Magnetocaloric Properties of $R_3Ga_5O_{12}$ (R = Tb, Gd, Nd, Dy), *Phys. Rev. Appl.*, 2023, **19**, 014038.

87 N. Terada and H. Mamiya, High-efficiency magnetic refrigeration using holmium, *Nat. Commun.*, 2021, **12**, 1212.

88 (*a*) CCDC 2504399: Experimental Crystal Structure Determination, 2026, DOI: **10.5517/ccdc.csd.cc2q212y**; (*b*) CCDC 2504400: Experimental Crystal Structure Determination, 2026, DOI: **10.5517/ccdc.csd.cc2q213z**; (*c*) CCDC 2504401: Experimental Crystal Structure Determination, 2026, DOI: **10.5517/ccdc.csd.cc2q2140**; (*d*) CCDC 2504402: Experimental Crystal Structure Determination, 2026, DOI: **10.5517/ccdc.csd.cc2q2151**; (*e*) CCDC 2504403: Experimental Crystal Structure Determination, 2026, DOI: **10.5517/ccdc.csd.cc2q2162**.

This journal is © the Partner Organisations 2026

Inorg. Chem. Front., 2026, **13**, 3170–3185 | **3185**